Satellite SAR interferometry for the improved assessment of the state of activity of landslides: A case study from the Cordilleras of Peru

Strozzi, Tazio ; Klimeš, Jan ; Frey, Holger ; Caduff, Rafael ; Huggel, Christian ; Wegmüller, Urs ; Rapre, Alejo Cochachin

Abstract: In Peru landslides have been causing damages and casualties annually due to the high mountain relief and distinct seasonal precipitation distribution. Satellite Synthetic Aperture Radar (SAR) interferometry represents one possibility for mapping surface deformation at fine spatial resolution over large areas in order to characterize aspects of terrain motion and potentially hazardous processes. We present land surface motion maps derived from satellite SAR interferometry (InSAR) for a part of the Santa River Basin between the Cordilleras Blanca and Negra around the city of Carhuaz in Peru. Using both Persistent Scatterer Interferometry (PSI) and differential SAR Interferograms (DInSAR) from ALOS-1 PALSAR-1, ENVISAT ASAR, ALOS-2 PALSAR-2 and Sentinel-1 we mapped 42 landslides extending over 17,190,141m² within three classes of activity (i.e. 0–2 cm/a, 2–10 cm/a and>10 cm/a). A geomorphological inventory of landslides was prepared from optical satellite imagery and field experience and compared to the InSAR-based slope-instability inventory. The two approaches provide slightly different information about landslide spatial and temporal activity patterns, but altogether they can be combined for the assessment of the state of activity of landslides and possibly the development of hazard maps, which are not systematically available in this region. We conclude that ALOS PALSAR (1 and 2) and Sentinel-1 data have a high potential to derive high-quality surface deformation information of landslides in many mountainous regions worldwide due to their global and frequent acquisition strategies.

DOI: https://doi.org/10.1016/j.rse.2018.08.014

Satellite SAR Interferometry for the Improved Assessment of the State of Activity of Landslides: A Case Study from the Cordilleras of Peru

Tazio Strozzi [1], Jan Klimeš [2], Holger Frey [3], Rafael Caduff [1],

Christian Huggel [3], Urs Wegmüller [1] and Alejo Cochachin Rapre [4]

[1] Gamma Remote Sensing, Worbstrasse 225, 3073 Gümligen, Switzerland

e-mail: {strozzi;caduff;wegmuller}@gamma-rs.ch

[2] The Czech Academy of Sciences, Institute of Rock Structure and Mechanics,

V Holešovičkách 41, Prague 8 182 09, Czech Republic

e-mail: jklimes@centrum.cz

[3] Department of Geography, University of Zurich, Winterthurerstrasse 190,

8057 Zurich, Switzerland

e-mail: {holger.frey;christian.huggel}@geo.uzh.ch

[4] Glaciology and Water Resources Unit (UGRH), National Water Authority (ANA), Huaraz, Peru

e-mail: jcochachin@ana.gob.pe

Abstract

In Peru landslides have been causing damages and casualties annually due to the high mountain relief and distinct seasonal precipitation distribution. Satellite Synthetic Aperture Radar (SAR) interferometry represents one possibility for mapping surface deformation at fine spatial resolution over large areas in order to characterize aspects of terrain motion and potentially hazardous processes. We present land surface motion maps derived from satellite SAR interferometry (InSAR) for a part of the Santa River Basin between the Cordilleras Blanca and Negra around the city of Carhuaz in Peru. Using both Persistent Scatterer Interferometry (PSI) and differential SAR Interferograms (DInSAR) from ALOS-1 PALSAR-1, ENVISAT ASAR, ALOS-2 PALSAR-2 and Sentinel-1 we mapped 42 landslides extending over 17,190,141 m^2 within three classes of activity (i.e. 0-2 cm/a, 2-10 cm/a and >10 cm/a). A geomorphological inventory of landslides was prepared from optical satellite imagery and field experience and compared to the InSAR-based slope-instability inventory. The two approaches provide slightly different information about landslide spatial and temporal activity patterns, but altogether they can be combined for the assessment of the state of activity of landslides and possibly the development of hazard maps, which are not systematically available in this region. We conclude that ALOS PALSAR (1 and 2) and Sentinel-1 data have a high potential to derive high-quality surface deformation information of landslides in many mountainous regions worldwide due to their global and frequent acquisition strategies.

Keywords

Satellite, SAR Interferometry, landslides, inventory, Peru.

1. Introduction

Landslides represent a major natural disaster causing fatalities and monetary losses in mountain regions worldwide, in particular where rapid development is increasing exposure of population and infrastructures. Landslide hazard assessment is an important aspect for disaster risk reduction with a direct impact on the use of the territory (Varnes et al., 1989; van Westen et al., 2008; Raetzo et al., 2002; Kunz & Hurni, 2008; Raetzo & Loup, 2016). Hazard is defined as the occurrence of potentially damaging natural phenomena of a certain intensity within a specific period of time in a given area (UNISDR, 2009; IPCC, 2014; Blaikie et al., 2014; Harb & Dell'Acqua, 2017). Hazard maps are based on two major parameters, intensity and frequency (or probability of occurrence). Because landslides are usually non-recurring processes, the return period has only a relative connotation and might rather be translated into probability of occurrence. Therefore, the determination of the class of intensity of landslides is often based on the state of activity and, in particular, on the velocity under the assumption that landslides are more hazardous if moving fast (Lateltin et al., 2005; Raetzo & Loup, 2016). The first step in landslide hazard assessment is to compile an inventory of landslides with a characterization of their typology (Varnes, 1978; Malamud et al., 2004; Lateltin et al., 2005; Guzzetti et al., 2012). This is commonly done based on field mapping, interpretation of aerial or satellite optical images, and information on historical events. In remote areas of high mountainous regions, high resolution optical satellite images can contribute to such inventory works by providing synoptic information about topography alongside with thematic information about terrain stability (Sato & Harp, 2009; Klimeš et al., 2015; Martha et al., 2016). By combining landslide inventory maps with ground displacement information, the state of activity of the mapped phenomena can then be evaluated (Raetzo & Loup, 2016). In absence of diffuse field data and mapping, satellite Synthetic Aperture Radar (SAR) interferometric approaches (Bamler & Hartl, 1998; Rosen et al, 2000) represent one possibility for mapping surface deformation at fine spatial resolution over large area. Since the launch of ERS-1 in 1991 it is

possible to use SAR interferometry (InSAR) to characterize aspects of terrain motion and related hazardous processes (Colesanti & Wasowski, 2006; Delacourt et al., 2007; Herrera et al., 2009). The available datasets have systematically expanded as new radar missions were launched, with more complete spatial and temporal information available (e.g. Notti et al., 2010; Strozzi et al. 2010; Barboux et al., 2015; Barra et al., 2017). Surface displacement rates quantified from InSAR are therefore increasingly used to derive the state of activity of mapped landslides (Farina et al., 2006; Bianchini et al., 2011; Righini et al., 2011; Cigna et al., 2012; Bianchini et al., 2013; Strozzi et al., 2013; Solari et al., 2018).

In Peru, landslides have been causing damages and casualties on an annual base due to the distinct seasonal precipitation distribution, accentuated by extreme rainfall events related to El Niño Southern Oscillation (ENSO). The average number of annual casualties by landslides during the 2004-2013 period was 35.7 for the entire country (Sepúlveda and Petley, 2015). In the Ancash Department, the annual landslide occurrence frequency of rainfall-triggered landslides and debris flows reported in the DesInventar database (DesInventar, 2018) for the period 1971-2009 was 9.2 (Vilímek et al., 2012). The same study (Vilímek et al., 2012) identified no landslides which initiation were related to earthquakes, even though during the 1996 - 2017 period the DesInventar database (DesInventar, 2018) described 30 earthquake events and the USGS earthquake catalogue (USGS, 2018) listed 59 earthquakes in this region. Two of them reached M 5.7, with one on 2010.01.03 located ca. 50 km north from Carhuaz. Nevertheless, none of the recorded earthquakes exceeded a IV surface shaking intensity on the Modified Mercalli Intensity (MMI) scale, showing their limited potential for landslide initiation. The very high potential of landslides causing economic damages in Peru can be illustrated by the rockslide affecting the Tablachaca Dam (Mantaro River) in 1974 and the debris flow from the Salcantay Mountain in 1998, which caused damage to the Machu Picchu hydropower plant. These two events resulted in about 200 million U.S. dollars in restoration costs (Deere and Perez, 1985; Reynolds, 2003). Therefore, there has been

a national-wide systematic effort of landslide inventory mapping and susceptibility assessment as a basic tool for mitigating landslide related damages and promoting sustainable land-use planning (Villacorta et al., 2012). This work includes reconnaissance mapping at 1:900,000 scale (INGEMMET, 2000; INGEMMET, 2002; INGEMMET, 2003; Fídel et al., 2006), which covers the Peruvian territory south of 10° latitude. Literature compilation, interpretation of aerial photographs and LANDSAT images, and field work at 1:250,000 scale, performed mainly along the major transportation roads, were used to prepare these maps. More detailed landslide and susceptibility maps were prepared for selected river basins and departments (Villacorta et al., 2012). The study for the Ancash Department (Zavala Carrión et al., 2009) contains a series of 1:250,000 landslide inventory maps prepared through field mapping at 1:50,000 scale and interpretations of historical aerial photographs and satellite images (LANDSAT and Google Earth). It resulted in the identification of more than 2000 hazardous events making part of the national-wide inventory of geological hazards, which contained 30,614 events in 2011 (Villacorta et al., 2012). Apart from this systematic and comprehensive mapping and inventory efforts, there are also within the Ancash Department studies providing local landslide information focusing on single events or river basins. The first landslide inventory which covered large part of the department was prepared by Plafker et al. (1971) after the 1970 earthquake. This work only provides an overview inventory map showing thousands of landslides in a point format. An inventory of 45 landslides triggered by the 1946 Ancash earthquake along with the analysis of their initiation conditions was published by Kampherm (2009). Another work describes selected cases of landslides in the Callejón de Huaylas region including those triggered by the strong 1998 ENSO anomaly (Vilímek et al., 2000). The most recent comprehensive work, which includes information about the spatial distribution of landslides on 1:50,000 maps, focused on the hazardous process related to the glacial environment between the Cordillera Blanca divide and the Santa River valley (Valderrama et al., 2016) using SPOT5 panchromatic images (Lacroix et al., 2013). Several geomorphological maps of glacial valleys in the Cordillera Blanca also show occurrence of basic landslide types, but have limited

spatial extent (Vilímek et al. 2005; Klimeš 2012). A systematic landslide susceptibility and hazard assessment map was prepared by Klimeš et al. (2015) for the Chucchún River basin using expert based landslide inventory and a hazard mapping approach. In addition, technical reports describing single recent landslide cases are being produced and published on-line by the civil protection office of Peru (INDECI, 2017).

Satellite SAR interferometry has been repeatedly used in the past in Peru for ground-motion monitoring related to earthquakes (Pritchard and Fielding 2008) and volcanoes (Jay et al. 2015), while landslides received much less attention. Gonzales et al. (2008) used ASAR and ERS images to investigate ground motion of six selected landslides in Peru, obtaining only partly satisfactory results due to the limited number of images, vegetation cover and low-resolution DEM from the Shuttle Radar Topography Mission (SRTM). Other remotely sensed images were used to determine ground motion of debris covered glaciers in the Cordillera Blanca, including matching of LANDSAT 7 ETM+ and LANDSAT 8 OLI images (Emmer et al., 2015) and unmanned aerial vehicle photogrammetry (Wigmore and Mark, 2017). Overall, there is a gap of comprehensive studies analysing the potential of satellite-based InSAR data for the investigation of landslide occurrence and hazard assessment for the Andes of Peru and other mountainous areas of the tropical Andes. In this paper we try to close this gap by presenting land surface motion maps derived from satellite InSAR in the surroundings of the city of Carhuaz (Ancash, Peru), discussing the potential and limitations of different satellite SAR sensors and processing approaches for the investigation of landslides in this area, and analysing how InSAR-based displacement information can be best combined with landslide inventories prepared from satellite optical images in order to assess the state of activity of landslides.

2. Study Area

Our study area is centered around the city of Carhuaz in the Ancash Region (Northern Peru), in the tectonic intermontane basin between the Cordilleras Blanca in the east and the Cordillera Negra in the west (Figure 1). This graben-like structure called Callejón de Huaylas drains into the Pacific Ocean by the Santa River, which has numerous tributaries running perpendicular to both ranges. The lowest and highest points of our study area are at 2,580 and 5,070 m asl (above sea level), respectively, whereas the highest peak of the Cordillera Blanca (Huascaràn) is at 6,768 m asl. The territory has steep slopes, usually between 20° to 30°, and is dissected by numerous deeply eroded gullies and small rivers. Two landslides located near the villages of Rampac Grande and Marcará, in the south and southeast of Carhuaz, respectively, are investigated in detail in this study. In particular, the most prominent landslide that occurred in this region during recent years is located above the Rampac Grande village on the southwestern Cordillera Negra side of the Santa River, which caused casualties and destroyed properties during the catastrophic failure event on April 25, 2009 (Klimeš & Vilímek, 2011).

[Insert Figure 1 about here]

The study area is characterized by the mild climate typical for tropical mountains. The annual average temperature varies between 11°C and 16°C depending mainly on the altitude. The annual precipitation ranges between 500 and 1,000 mm and the precipitation pattern is affected by seasonal shifts of the Intertropical Convergence Zone (Kasser et al., 1990). The dry period typically lasts from May to September, whereas the rainy season lasts from October to April. Snow cover is only present on the highest glacierized peaks of the Cordillera Blanca and is thus not disturbing the analysis of the satellite SAR images in our study region. The rocky peaks on the Cordillera Negra have very little snowfall. Vegetation cover is not dense, in particular over the Cordillera Negra (MINAM, 2015). The two cordilleras host at lower elevation xerophytic shrubs adapted to the

intense solar radiation and are surrounded by grasslands and sparsely occurring forests in the middle and higher elevations. The main economic activities in the area are tourism and agriculture, with growing of wheat, maize, oats and fruits on terraced fields. Quarries and underground mining activities affect only limited parts of the study area but may have significant influence on land surface characteristics.

The graben like structure of the Callejón de Huaylash originated during the Early Pliocene and Holocene through tectonic movements in Mesozoic and Tertiary sediments and volcanites, which are filling this depression to the depths of up to 2 km. The basement rocks of Mesozoic age (Figure 2) comprise folded metasedimentary rocks of the Middle-Upper Cretaceous age. These rocks of siliclastic and carbonate compositions (Goyllar Group and Parihuanca Formations) contain limestone, shale, mudstone, claystone, sandstone, and conglomerate (INGEMMET, 1995; Weston, 2008). The basement rocks are conformably overlain by the flat-lying intermediate to felsic tuffs and flows of the Calipuy Group (Weston, 2008). These rocks are intruded in places by stocks of Neogene age volcanic rocks, which are likely to be genetically related to the contemporaneous intrusion of the granodiorite batholith of the Cordillera Blanca (Miocene age). The sequence is also locally overlain by tuffs of Pliocene age, termed the Yungay Formation (Weston, 2008). The Cordillera Blanca normal fault with a total length of 210 km limits the graben on the west side and it is considered active. The long-term vertical displacements during the last 2.8 Ma on the section of the fault in the study area are mostly smaller than 3 mm/a. The geologically evidenced movements (e.g. offsets of glacial deposits) are younger than 15 ka and there are no historical earthquakes recorded (Macharé et al., 2003). Several hot springs (e.g. Chancos 3.5 km east from Marcará with water up to 70°C) are located along the fault. Other faults are represented by disharmonic anticlines and synclines in both the metasedimentary basement and overlying igneous rocks with axes generally following the north-western Andean trend. The high seismicity of this region is strongly related to the Pacific Plate subduction (Bernal et al., 2002) and is reflected by high probabilities of

earthquakes reaching shaking intensities larger than VII MMI close to the coastline (Petersen et al, 2017).

[Insert Figure 2 about here]

3. Data and Methods

3.1 Satellite SAR interferometry

We generated a consistent data set of differential SAR interferograms (DinSAR) with stacks of ERS-1/2 SAR, ENVISAT ASAR, ALOS-1 PALSAR-1, TerraSAR-X, Radarsat-2, ALOS-2 PALSAR-2 and Sentinel-1 images acquired between 1992 and 2017 from ascending and descending orbits (Table 1). The acquisition time intervals of the differential interferograms ranged from 1 day to about 5 years. For topographic reference (Bamler and Hartl, 1998; Rosen et al., 2000) a DEM was generated from TanDEM-X acquisitions performed along ascending (24.01.2013) and descending (01.10.2013) orbits combined to reduce problems of areas masked by layover and shadow which affect differently opposite slopes along north-south oriented valleys in mountainous regions. The DEM was produced with a posting of 0.0001 decimal degrees, corresponding to about 10 m. TanDEM-X DEMs produced with the same methodology in the past over Mount Etna in Italy (Wegmüller et al., 2014) and the Chomolhari region in Bhutan (Ambrosi et al., 2018), regions with comparable topography as our study area, were validated against ground control points. In comparison to more than 100 GPS benchmarks over Mount Etna and 10 GPS survey points in the Chomolhari region mean differences of the elevations of 0.6 m and 3.6 m, respectively, and standard deviations of 4.3 m and 2.8 m, respectively, were found. Major limitations to the application of DInSAR in mountainous areas arise from layover and shadow effects as well as from

phase decorrelation caused by snow cover at higher elevations and vegetation cover at lower elevations, in particular at C- and X-bands (Strozzi et al., 2013).

Persistent Scatterer Interferometry (PSI) analyses (Ferretti et al., 1999; Wegmüller et al., 2003) were conducted with the stacks of ENVISAT ASAR images of the descending orbit (21 acquisitions), the ALOS PALSAR images of the ascending orbit (19 acquisitions) and the Sentinel-1 images of the ascending (35 acquisitions) and descending (45 acquisitions) orbits. For the other image stacks (see Table 1) the number of acquisitions was not sufficient for this type of processing. Reference points were selected individually for each of the sensors in presumably stable areas. Isolated anomalous displacements or displacements greater than 3 mm/a, 5 mm/a and 20 mm/a for ENVISAT ASAR, Sentinel-1 and ALOS-1 PALSAR-1, respectively, were filtered. PSI results consist of linear deformation rates and displacement histories in the satellite Line-Of-Sight (LOS) direction. In the past, the accuracy of PSI results was estimated for stacks of SAR images acquired with sensors, time spans between the first and the last scene, sampling intervals, and number of acquisitions similar to those selected for our study. While the limit of accuracy of PSI with ENVISAT ASAR data is between 1.0 to 1.8 mm/year over a time period of 5 years for the average displacement rate and between 4.2 and 6.1 mm for single deformation measurements (Crosetto et al., 2009), that of PSI with ALOS-1 PALSAR-1 over a time period of 4 years is on the order of 9 mm/year for the deformation rate (Ng et al., 2012) and of 14 mm for single measurements (Sandwell et al., 2008). For Sentinel-1 images no quality indications have been published so far, however, over a time period of two to three years, we expect a reduced accuracy of the average displacement rate (e.g. a few mm/year) compared to that determined with the ENVISAT ASAR data. For ALOS-2 PALSAR-2 Nishiguchi et al. (2017) found that the average difference between the displacements obtained by DInSAR analysis and field measurements by GNSS was 15.1 mm in the LOS direction.

[Insert Table 1 about here]

3.2 InSAR-based slope-instability inventory

By the visual analysis of the ALOS-1 PALSAR-1 and ENVISAT ASAR PSI surface displacement maps and the series of ERS-1/2 SAR, ENVISAT ASAR, ALOS-1 PALSAR-1, TerraSAR-X and Radarsat-2 DInSAR images, we detected regions with high surface movement rates. Because this inventory does not only include landslides, we call it slope-instability inventory. Interpretation of the wrapped interferometric signals was performed following the recommendations given in Barboux et al. (2014) in order to locate and estimate the displacement rates of moving zones. In the DInSAR images we estimated the errors due to atmospheric distortions and noise in the order of ¼ of a phase cycle (Strozzi et al., 2001). Following the rules proposed for Switzerland (Raetzo & Loup, 2016), the magnitude of the detected moving rates was classified into three classes: 0-2 cm/a, 2-10 cm/aand >10 cm/a. In cases where the derived velocity was close to the upper velocity boundary, the polygon was classified using the faster class. The same effect applies to natural variations of the surface displacement rates. If two or more classes were present in the observation time-span, the higher velocity rate was used to determine the velocity class. Because the InSAR derived displacement rates are measured along the satellite LOS, the actual landslide movement is underestimated. The SAR derived displacement rates measured along the LOS could be re-projected into a new velocity along the steepest slope direction for a more throughout interpretation (Bianchini et al., 2013). In our analysis, however, the LOS was only empirically considered in the assessment of the state-of-activity of the mapped landslides.

Visual interpretation of very-high resolution optical satellite images from Google Earth (images dating 2012 and 2013) and Bing (image dates unknown, access date January 2015) was then used for geomorphological interpretation of the ground surface movements, attributing them to specific

landforms and natural or anthropic surface processes. Regions with high surface movement rates were classified as landslides, moraines, rock glaciers, dead ice, ground settlements, and mining affected areas. The optical images allowed for more precise and comprehensive mapping of the entire features including parts which do not exhibit ground surface movement but belong to the same landforms. Therefore, the InSAR slope-instability inventory is based on a combination of expert-based interpretation of PSI and DInSAR data and landslide mapping using remotely sensed optical imagery. Automatic approaches to extract clusters of moving areas from the PSI dataset would permit mapping active deformation areas without manual visual analysis (Barra et al., 2017; Solari et al., 2018). However, such an automatic procedure would still need to be complemented by the visual analysis of DInSAR data for fast movements not detectable with PSI and of optical imagery for geomorphological interpretation of the ground surface movements, because no complete landslide inventory is available in our study area. Therefore, this approach was not considered in our analyses.

3.3 Geomorphological landslide inventory

A geomorphological landslide inventory was prepared through interpretation of optical satellite images available from Google Earth (Fiorucci et al., 2011) and considering field experience from previous works in the study area. The principle aim of the geomorphological landslide inventory was to cross-validate the InSAR-based slope-instability inventory through mapping all landslides within the study area. However, when combined with InSAR terrain motion data to improve the assessment of the state of activity of the landslides, the geomorphological landslide inventory can be also considered to compile hazard maps.

The geomorphological interpretation was done mostly based on the Google Earth July 2016 image due to its good quality and image contrast, but other historical images were also considered in order

to obtain multi-temporal information about landslide occurrences and activity. The intervals between subsequent images available on Google Earth are restricted to a few years and imagery before 2003 is not available, putting constraints on the identification of the main reactivation phases or landslide initiations. The geomorphological inventory provides definitions of the types of landslides based on forming process, state of activity, depth of the main sliding surface and sliding plane geometry. The state of activity was defined purely using the appearance of the landslide - fresh looking landforms (clearly visible and sharp scarps, bare surface) were assigned as “active” (McCalpin, 1984; Wieczorek, 1984). Other landforms where vegetation or denudation obscured the surface landforms were assigned as “temporarily inactive”. This “activity” definition does not follow the international standards (e.g. Varnes, 1978), but provides a proxy indication of the possible state of the landslide movement activity, suggesting that freshly looking landforms may result from repeated or continuous small scale movements, whereas the masked landslides suggest that the region has been without important gravitational movement for long periods of time. Such activity identification has serious drawbacks. For instance, it is not capable of accounting for small scale movements which do not disturb the land surface and its cover, as in the case of some deep seated landslides. On the other hand, this approach is consistent with the InSAR information which reflects only the surface movements. The depth of the sliding surface was classified as “shallow” (less than 2 m), “medium” (2 to 10 m) and “deep” (more than 10 m), using the height estimation of the main scarp and assuming a mostly planar or, when evidences of counter-slope rotation below the main scarp were identified, semi-circular sliding surface geometry. The landslide description needs to be considered with caution keeping in mind that field survey is necessary to get reliable, site specific information with respect to landslide hazard assessment. Approximately 50% of the geomorphological landslide inventory was checked in the field in May 2017. The geological units (Figure 2) were reclassified into three lithological classes to evaluate the conditions of the landslide occurrences. The sedimentary rock class contains the Santa and Pariahuanca formation and the Goyllar group. The volcanic rock class is formed by Yungay formation and Calipu group. The third

class is represented by fluvio-glacial deposits. Landslides were attributed to the individual lithological group based on the location of their source areas.

4. Results

4.1 Satellite SAR interferometry

In Figure 3, we present the results of the PSI analyses of the ALOS-1 PALSAR-1, ENVISAT ASAR and Sentinel-1 data. In the PSI average displacement rate maps, negative values indicate an increase in the distance from target to satellite or, in general, a lowering of the surface. A comparison of Figures 3a and 3b and the standard statistics computed for each of the PSI results (Table 2) indicates that the point density obtained with ALOS-1 PALSAR-1 is much higher than that obtained with ENVISAT ASAR. The generally sparse vegetation cover is largely precluding successful PSI analysis with C-band data acquired with a repeat time of 35 days. Only at very-high altitudes close to the glaciers and over the build-up areas, there is a good density of information from ENVISAT ASAR. In addition, by reason of the steep incidence angle of ENVISAT ASAR (23°) the areas masked by layover and shadow in Figure 3b are very extended. Most of the slope instabilities classified in the inventory are thus derived from the interpretation of the signals visible in Figure 3a. Only in the north-eastern section, there is a cluster of moving points visible in the ENVISAT ASAR PSI analysis. Here, the rates of movement detected with ALOS-1 PALSAR-1 is close to zero or even slightly positive (blue points), pointing out to an unfavourable satellite LOS rather than to a reduced activity during 2007-2011 compared to 2002-2007.

Sentinel-1 PSI results are presented in Figures 3c and 3d for images acquired along the ascending and descending orbits, respectively. The results obtained with the 45 descending images acquired

between 2014 and 2017 early in the morning are less affected by atmospheric artefacts than those obtained with the 35 ascending images acquired between 2015 and 2017 late in the afternoon, possibly because of the larger number of scenes, the longer observation interval or a more favourable time of acquisition. Therefore, the standard deviation of the average annual motion rate (Table 2) is smaller for the results obtained along the descending orbit (2.35 mm/a) than along the ascending orbit (2.96 mm/a) and the colour scale used in Figures 3c and 3d is not the same. The point density obtained with C-band data acquired with a repeat time of 12 to 24 days is very high (Table 2), but with our processing we could detect few points with comparatively high rate of motion (> 2 cm/a). Overall, the Sentinel-1 results are comparable with those from ALOS-1 PALSAR-1 (Figure 3a) and ENVISAT ASAR (Figure 3b). In particular, with descending orbit Sentinel-1 data (Figure 3d) the cluster of moving points in the north-eastern section of the study area is very clearly defined. Over the Cordillera Negra between the Rampac Grande and Marcará landslides, around location f in Figure 3d, most of the points detected with Sentinel-1 along the descending orbit are showing a positive LOS rate of motion because of the satellite viewing geometry.

[Insert Table 2 about here]

[Insert Figure 3 about here]

In addition to linear deformation rates, PSI results consist of displacement histories in the satellite LOS direction. Six representative movement histories are shown in Figure 4, illustrating different landslide dynamics in the study areas. A steady rapid movement between 2007 and 2011, which can be related to lateral erosion by the Santa River, is observed within the Marcará landslide with ALOS-1 PALSAR-1 data (Figure 4a, for location see Figure 3). On the other hand, the time-series for the same data set on a point more to the north-west (Figure 4b) indicates movement only around 2009, a year with extreme precipitation totals during the rainy season (Klimeš and Vilímek, 2011).

Permanent motion is also observed with ENVISAT ASAR data within the cluster of moving points in the north-eastern section of the study area (Figure 4c). For the study of repeated seasonal dynamics, the sampling rate of the past ALOS-1 PALSAR-1 and ENVISAT ASAR is unfortunately too coarse. An example of a sudden change in the movement behaviour at the end of the rainy season can be observed for one point with ENVISAT ASAR data only around 2005 (Figure 4d), when more images were acquired. Sentinel-1, with its consistent acquisition strategy, is much more suitable for the analysis of such seasonal signals. Sentinel-1 time-series from the ascending and descending geometries for points located within an area with high rates of movement are presented in Figures 4e and 4f, respectively. These high movement rates are likely caused by soil sheet erosion during the rainy season, because the fine grained sediment/soil surface is not protected from being washed away during intense precipitation events. In both time-series, we recognize periods of inactivity around the austral winters of 2016 and 2017 (dry season) and accelerations during austral summers of 2016 and 2017 (rainy season), caused by increased erosion rates. Prior to 2016, Sentinel-1 acquisitions were sparser and the time series more inaccurate, in particular for the ascending orbit with a phase unwrapping error for the first point. The different sense of motion of the plots of Figures 4e and 4f are the effect of the line-of-sight direction with respect to the slope orientation of the satellite images of ascending and descending orbits.

[Insert Figure 4 about here]

4.2 InSAR-based slope-instability inventory

The polygons of the InSAR-based slope-instability inventory are also shown in Figure 3, classified according to the rate of movement. In addition to the three velocity classes 0-2 cm/year, 2-10 cm/year, and >10 cm/a, we introduced an “undefined” velocity class in the case it was not possible to clearly assign a magnitude of displacement to a well defined landslide, e.g. because of layover,

shadow or strong decorrelation. The inventory extends beyond the study area described in this paper, as the coverage of the SAR images is larger. However, our discussion is restricted to the regions where the geomorphological landslide inventory was accomplished (white dashed polygons in Figure 3). In addition, it has to be considered that the slope-instability inventory was elaborated considering only results obtained from ALOS-1 PALSAR-1 and ENVISAT ASAR PSI analyses, because ALOS-2 PALSAR-2 and Sentinel-1 data were processed at a later point. Within the study region the InSAR-based slope-instability inventory contains 42 landslides, one area with potential ground settlement, and three objects showing continuous-type movements, which could not be classified with the available datasets. In total, 17,190,141 m^2 were classified in an active state of motion, of which 16,513,839 m^2 were identified as continuously active landslides and 263,159 m^2 as episodic active landslides. With respect to the state of activity, 4 instabilities were classified with a rate of motion >10 cm/a, 22 between 2 and 10 cm/a and 10 between 0 and 2 cm/a. Six landslides were categorized as “undefined”.

As it can be observed in Figure 5a, there are four polygons of the slope-instabilities inventory with rate of motion >10 cm/a where no information is available from the PSI analyses. In these cases, the velocity of movement was detected from the analysis of differential SAR interferograms. The example of Figure 5c for the time period 2009.07.17-2009.09.01 (46 days) indicates four clear signals (1 to 4) with a purple or yellow colour, corresponding to a movement of more than about 4 cm. In addition, also in the small region above the April 2009 Rampac Grande landslide scarp (Klimeš & Vilímek, 2011) this interferogram captures a small movement activity (number 5 on Figure 5c), probably representing a re-adjustment of the slope above the fresh landslide. In Figure 5b a previous interferogram also spanning 46 days during the time period 2007.07.12-2007.08.27 is only showing minor signals related to movements in these areas. A more recent ALOS-2 PALSAR-2 interferogram for the time period 2016.02.21-2016.10.02 (224 days, Figure 5d) shows activity in certain sites, but with decreased magnitude compared to 2009. Recent activity is particularly

evident for locations 2 and 3 near the Rio Santa, which are being actively eroded. On the other hand, for site 1 detected in the 2009 image in the north-west there was no activity in 2016, suggesting that the movement was related to high precipitation in the 2008/2009 rainy period. None of these sites (1, 2 and 3 on Fig. 5) was identified during the geomorphological mapping (including the field surveys), highlighting how useful the information from satellite SAR interferometry is for the identification of slow-moving landslides. Location 4 is disconnected form the Santa Valley and there is only a small tributary with no pronounced deep-ward erosion. The high movement rate is likely caused by soil sheet erosion during the rainy season.

[Insert Figure 5 about here]

4.3 Geomorphological landslide inventory

The geomorphological landslide inventory is presented in Figure 6. In total, 27% of the study area is covered by landslides (Table 3). Active and temporarily inactive shallow landslides with planar sliding surface are the most frequent ones (41% of the mapped landslide cases), even if they cover less than 8% of the total mapped landslide area. On the other hand, temporarily inactive landslides with deep sliding surface account for only 9% of the individual landslides but represent 57% of the landslide area. Debris flows constitute only a very limited portion of the identified landslides (14%) and landslide area (5%). Active landslides and debris flows, which constitute a minor part (12%) of the landslide covered slopes, often occur close to gullies on steep slopes. Landslides (active or temporarily inactive) with medium deep planar or semi-circular sliding planes cover 30% of the landslide area, the second largest mean sliding area. Large size landslides are in many cases deep and were identified mainly in the north part of the study area where the small size landslides are much less abundant than in the rest of the study region. During the field check performed for 113 landslides mapped through satellite image interpretation, several new landslides (5% of the total

number of the checked landslides) were mapped and some others (13% of the total number of the checked landslides) were not confirmed or their delimitation was modified.

The lithological division of the study area is very general and only partly reflects the variability of the geological conditions as the sedimentary class contains a large variety of rocks (e.g. limestone, shale, mudstone, claystone, sandstone, and conglomerate). The sedimentary class also covers the majority of the studied area, so 81% of the mapped landslides developed on this lithological class. From the 13% of the landslides which occurred within the volcanic lithology, 62% are shallow, active or temporarily inactive landslides with planar sliding plane. The rest are constituted by landslides with medium or deep sliding surface, while debris flows are absent within this lithological unit. Less than 6% of identified landslides developed on glacio-fluvial sediments which rim the foot of the Cordillera Blanca range.

[Insert Table 3 about here]

[Insert Figure 6 about here]

5. Discussion

5.1 Potential and limitations of satellite SAR interferometry for the assessment of the state of activity of landslides

The use of PSI and DinSAR for land surface displacement maps largely improves the assessment of the state of activity of landslides as compared to the strictly geomorphological approach. Satellite SAR interferometry is able to cover wide areas and does not require field work and installation of in-situ fixed points which in some places may be affected by adverse environmental conditions or

vandalism. Useful information from this technology can be obtained in built-up and sparsely vegetated areas. For our study area in the Cordilleras of Peru the use of L-band SAR data allowed us to achieve a remarkable high density of valid information. C-band results, on the other hand, are less complete in terms of spatial coverage, in particular with ENVISAT ASAR data characterized by an irregular acquisition sampling interval. Landslides with a comparably large rate of movement (i.e. larger than 2 to 3 cm/a) and with strong seasonal variations cannot be detected by use of PSI, but in many cases they can be observed using single differential interferograms. Topography is limiting the application of this technology, in particular due to geometrical limitations related to layover and shadow. Areas masked by layover and shadow shown in Figure 3 are larger for ENVISAT ASAR compared to ALOS-1 PALSAR-1 and Sentinel-1 because of the steeper incidence angle (~23° versus ~35°, respectively). Another aspect related to the topography and the special SAR viewing geometry is that PSI and DInSAR data are only sensitive to movements taking place along the satellite LOS direction. If the LOS orientation is not favourable in relation to terrain deformation, the number of detected points might be reduced. Using images acquired along both ascending and descending orbits can in principle reduce this problem. However, over our study region ALOS-1 PALSAR-1 data were mainly acquired along the ascending orbit only, while ENVISAT ASAR images were principally taken along the descending orbit. Using Sentinel-1 data, which are consistently acquired on both orbits, reduces these inconveniences. Based on our analyses it is evident that best results are achieved by the complementarity use of different acquisition geometries, different sensors (with regard to wavelength and resolution) and different processing approaches (PSI and DinSAR).

PSI time-series of motion can be used to track changes in the rate of motion, for instance by comparing the annual dynamics of different years to see if there are repeated movement patterns. Acceleration of certain points or areas can indicate a critical situation requiring field surveys or can be a result of episodic movements caused by extreme precipitation conditions, as illustrated by the

time series on Figure 4b for the year 2009. A prerequisite for this kind of analysis is a high temporal sampling of acquisitions over several years, as currently available with the Sentinel-1 constellation. Past ALOS-1 PALSAR-1 and ENVISAT ASAR images are more limited for these investigations over the Cordilleras of Peru. With a small number of acquisitions, as it is the case over our study area with ERS-1/2, TerraSAR-X and Radarsat-2, very little information can be retrieved from SAR interferometry.

5.2 Cross-comparison of the InSAR-based slope-instability and geomorphological inventories

The InSAR-based slope-instability inventory and the geomorphological inventory previously discussed are obtained by different approaches. The InSAR slope-instability inventory is mainly derived from the motion observed with PSI and DInSAR data, which are interpreted as slope-instability areas with the support of satellite optical data and a DEM. Outside the DInSAR coverage, only very obvious landslides are considered in this inventory. The geomorphological inventory, on the other hand, was prepared using optical satellite images and in-depth field experience. Hence, the two inventories were prepared independently and do not represent the same information. The InSAR-based slope-stability inventory identifies only features with observed surface movements and misses landslides temporarily without movement activity or not appropriate to be analysed with the InSAR technology, e.g. because of rapid and sporadic rate of motion or masked by shadow or layover. On the other hand, the geomorphological mapping tends to overlook some actively deforming features, which lack significant morphological imprints and has limitations in estimating recent movement activity of individual landslides. Thus, rather than strictly validating one inventory with the other, we compare them to enhance the understanding of slope deformation processes in the field. We do so analysing the inventories over two selected parts of the study area, i.e. between the Rampac Grande and Marcará landslides (Figure 7) and on the north-east(Figure 8). In the following section, we will investigate how the two approaches can be

best combined in order to assess the state of activity of landslides and possibly inform the development of hazard maps.

In Figure 7 the spatial distribution of the clusters of PSI points in regions 1, 2 and 3 with rates of movement larger than 1 cm/a indicates landslide occurrence. The most active landslides, i.e. the landslides that are active almost every year, are affected by lateral erosion by the Santa River. Time-series of ALOS-1 PALSAR-1 (e.g. Figure 4a) and Sentinel-1 data can be considered for a reconstruction of the displacement history, generally showing continuous movement. The clusters of points labelled with 1 and 2 in Figure 7 are to the west and east, respectively, of the Rampac Grande landslide. To the north-east of region 1 three small polygons with strong activity were classified according to the 2009.07.17-2009.09.01 ALOS-1 PALSAR-1 interferogram (Figure 5c) and may be interpreted as postponed results of the above average precipitation of the 2009 rainy season. To the north of region 2 the 2009.07.17-2009.09.01 interferogram also showed a strong activity in a zone which was not first identified during the geomorphological mapping (location 3 in Figure 5c). However, careful analysis of the Google Earth images showed a very subtle linear vegetation feature, which may be considered as a continuation of a clearly developed scarp combined with high erosion of the Santa River. Field checks in May 2017 confirmed repeated sliding activity including newly developed opened cracks in its scarp area related to the rainy season 2016/2017.

The deformations detected in the region number 3 (Figure 7) corresponds to the activity within the Marcará landslide, although this landslide was mapped as temporally inactive during the Google Earth image interpretation since it lacks surfaces with exposed rocks and clear tension cracks. However, the general morphology of the Marcará landslide corresponds well with a deep-seated landslide. Its main scarp is formed by narrow ridges and cuts across a ca. 600 m high mountain where two medium-deep rockslides developed. There are several platforms with shallow, down-

slope inclination below the main scarp. The landslide body in the area 3b is disintegrated by partial scarps (about 10 m high) close to the river, where several well defined shallow landslides developed. Similarly, high PSI velocities are observed for areas 3a and 3b, but the field observations suggest that the landslide activity, with the presence of more shallow, partial landslides and scarps, increases towards its southeast limit (3b on Figure 7). Therefore, the movements in region 3a can be mostly related to the steep gully slopes and shallow landslides on the steep erosional slope of the Santa River.

The band of increased velocities to the south of the Marcará landslide (number 4 on Figure 7) forms on steep slopes with gullies and the spatial distribution of points does not follow or suggest the presence of a landslide body. Here, PSI movements might be related to superficial denudation processes on steeper slopes. Slightly to the north of region 4, a signal in the 2009.07.17-2009.09.01 ALOS-1 PALSAR-1 interferogram and high rates of motion from the Sentinel-1 PSI analyses (Figures 4e and 4f) are possibly indicating soil sheet erosion during the rainy season. In this area no landslides were mapped in the geomorphological inventory of Figure 7b, but polygons are included in the InSAR-based slope-instability inventory of Figure 7a.

[Insert Figure 7 about here]

Mostly deep-seated and large landslides on glacio-fluvial sediments were identified in the north-eastern part of the study area, where the PSI analysis of ENVISAT ASAR (2002-2007, Figure 8a) and Sentinel-1 (2014-2017, Figure 8b) data indicate significant motions. The InSAR-based slope instability inventory was elaborated considering only ENVISAT ASAR and ALOS-1 PALSAR-1 data, therefore the extend of the moving areas 1 and 2 in Figure 8 was underestimated. A field visit in 2015 provided clear evidence of active landsliding along the local stream which undercuts the toe of both landslides. On the other hand, no morphological evidence of continuous movements was

found further away from the river below their scarps, as indicates especially the Sentinel-1 PSI results (number 2 in Figure 8b). Movements detected north from area 1 in Figure 8 are related to several small scarps on moraine ridge disrupted by the Cordillera Blanca normal fault. This region was not identified as landslide, because it lacks a clearly defined landslide morphology (e.g. missing landslide body and accumulation area). However, the PSI rates of motion suggest that the moraine deformations are most likely related to gravitational processes rather than to the fault movement activity, because long-term slip rates based on the fission track dating for this portion of the Cordillera Blanca fault only range from 0.9 to 1.9 mm/year (Macharé et al., 2003).

[Insert Figure 8 about here]

5.3 Landslide hazard assessment

Landslide hazard assessment allows an improved knowledge of the territory with direct consequences to the land-use management and disaster risk reduction. A landslide hazard map indicates the spatial (i.e. susceptibility) and temporal probabilities of landslide occurrences or major reactivations as well as the intensity of the expected movements (Varnes et al., 1989; van Westen et al., 2008; Raetzo & Loup, 2016). The InSAR-based slope-instability and geomorphological inventories that we created for the Carhuaz region in Peru have a high potential to be jointly considered in the preparation of a hazard map for the common area covered by both inventories. In the following, we outline a few aspects relevant for the development of a landslide hazard map based on our investigations. A final hazard map was, however, not created because it would require a more thorough analysis of the whole territory and available data with all their peculiarities.

The first step in landslide hazard assessment is the compilation of a susceptibility map. Since the geomorphological inventory was aimed to identify all landslide features within the study area and

included field check, it is considered the primary source for susceptibility mapping. However, areas where the InSAR-based inventory identified movements which were not captured by the geomorphological mapping should be double checked using in-depth examination of the optical satellite images or during field work. This helps to identify landslides previously overlooked during the geomorphological analysis, e.g. because masked by human activity. On the other hand, regions with significant DInSAR signals may be disregarded if no clear morphological evidences about landslide occurrence can be found. This could mean that the observed surface movements are caused by other processes (e.g. subsidence, soil erosion or mining).

For the intensity component of a hazard map one possibility is to only consider mean annual velocities following the approach used for the Swiss intensity/velocity classification (Raetzo & Loup, 2016), which assumes that landslides are usually non-recurring processes. However, this approach might be adapted based on regional specific conditions (i.e. dry/wet season with landslide re-activations). Using the available data the landslide hazard can be divided in three classes according to mean annual velocities below 2 cm/a, between 2 and 10 cm/a and above 10 cm/a. For regions without DInSAR data the estimation of the movement activity of the landslides is sometimes possible from the geomorphological analysis, but often other criteria, such as similarity of the landslides to other already classified (Ambrosi et al., 2018) or based on slope stability models (Moon and Blackstock, 2004), need to be adopted. With newest satellite missions providing regular acquisitions over longer time periods (e.g. Sentinel-1 with a 12-days nominal repeat interval since 2016 over Peru) it is also possible to frequently update the DInSAR results.

DInSAR has thus the potential to significantly improve the hazard defined based on geomorphological mapping only, but it still provides only a proxy for possible activity of deeper sliding planes. In the case of absence of any monitoring data, the only possibility to reduce this uncertainty is an expert, in-depth evaluation of the landslide morphology with respect to how well it

may reflect sliding processes at depth. An example is the Marcará landslide (Figure 7), where the field monitoring identified well developed partial scarps within the most extreme southeast portion of region 3b. Therefore, we may assume that the DInSAR deformations most probably reflect movements along sliding planes. Such morphological evidence is missing in the central and northern parts of this landslide (3a), thus the link between observed surface deformations and sliding activity is here largely speculative. This detailed morphological evaluation is difficult to perform over large areas, so the hazard map has to assume a direct relationship between InSAR deformations and movements along sliding planes considering that in the most cases the reactivation propagates from depth to the surface.

6. Conclusions and Outlook

An intensive, multi-sensor satellite InSAR analysis of surface displacements was performed in the upper Santa Catchment in the Andes of Peru, where frequent landslide occurrence is often related to significant damage, information about landslide movement activities is scarce, and detailed landslide inventory maps are generally not available. Our results prove that in regions with sparse vegetation cover and absence of snow cover InSAR is highly suitable to (i) identify actively moving landslides, (ii) indicate their state of activity (or velocity class), and (iii) describe deformation histories over specified time periods. We found that the removal of material at the toe of various landslides by river erosion is a key factor for the long-term movement activity. On the other hand, landslides outside the reach of the effects of river erosion do not exhibit frequent movement activity but reactivate mainly due to precipitation events, like the extremely wet 2008/2009 rainy season. All available satellite SAR data were considered in our analyses, but PSI and DinSAR results obtained from the ALOS PALSAR (1 and 2) and Sentinel-1 sensors have the highest quality for landslide studies, mainly because of their operational wavelengths and sampling intervals,

respectively. These sensors have a particularly high potential to derive surface deformations caused by landslides also for other mountain areas worldwide, but have not consistently exploited in order to manage, mitigate and avoid related hazards in typically vulnerable, populated mountain areas. Correlations of optical satellite images (Lacroix et al., 2013; Lacroix et al., 2015; Stumpf et al., 2017; Bontemps et al., 2018) would permit remote-sensing detection of landslides moving faster (e.g. >1 m/a), which are hardly detectable with satellite SAR sensors, ideally complementing InSAR results.

Collecting landslide surface deformation information using in-situ methods at comparable spatial scales would be extremely time and cost intensive. Thus, InSAR represents a highly valuable source of information for a reliable landslide hazard assessment. However, our work also showed that thorough field investigations are required in order to correctly interpret InSAR-based information for landslide hazard assessments. Without independent geomorphological evaluation, an InSAR-based landslide inventory would miss landslides with fast surface deformation or with superficial movements on steep slopes. In addition, InSAR only provides surface deformation and there is a questionable link between the activity at the surface and that of the deeper sliding planes. On the other hand, slow-moving landslides can be easily overlooked in the geomorphological analysis due to their featureless morphology. Hence, the combination of the geomorphological and InSAR-based landslide inventories has mutual benefits, preventing to oversee areas with unfavourable conditions for infrastructure constructions or sources of potentially catastrophic landslides. We presented a unique evaluation in Peru of a possible combination of InSAR and expert-derived landslide information, which overcomes the obstacle of collecting regional wide, reliable and detailed geological or soil factor maps. The two approaches provide slightly different information about landslide spatial and temporal activity patterns, but altogether may result in comprehensive and reliable hazard information. Increasing availability of SAR and optical satellite data create favourable conditions for the preparation of such methodology in high-mountain regions worldwide

where information about distribution of landslide preparatory/conditioning factors which control their spatial and temporal occurrence are largely unavailable, but more in-depth evaluation is still needed.

In order to validate the Sentinel-1 PSI results, field monitoring of the landslides of Rampac Grande and Marcará (Figures 1 and 2) has been recently initiated. Two extensometric profiles of 18 stainless steel tubes, inserted more than 1.5 m into the ground, were deployed in July 2016 over the Rampac Grande landslide in order to describe the movement activity of two partial landslides in highly unstable conditions (Vilímek et al., 2016; Klimeš et al., 2017). Over the entire Marcará landslide, 13 concrete-embedded survey points were marked in May 2017 for repeated tachymetric surveys. In both cases, a measurement period of two to three years is required for obtaining reliable information of slope deformations (Zvelebil and Stemberk, 2000). A major advantage of InSAR is thus the rapid availability of quantitative slope deformation information, for both actual conditions as well as periods in the past.

Finally, and related to landslide hazard assessment, the potential of InSAR data should be mentioned for the early warning of landslides. There exist a substantial number of studies that analysed how space-borne SAR data can be used for landslide early warning (e.g. Casagli et al. 2017), although little experience is available for the developing world such as for Peru. Furthermore, there is a lack of integration into operational early warning systems, which poses important challenges to data processing (Huggel et al. 2017). We therefore suggest to further develop methods for the use and for the integration of InSAR data in operational landslide early warning systems.

Acknowledgments

The research leading to these results received funding from the European Space Agency (ESA) within the S:GLA:MO (Contract No. 4000110404/14/F/I-BG) and ALCANTARA (Contract No. 4000117655/16/F/MOS**)** projects and support from the long-term conceptual development research organization RVO:67985891. ENVISAT SAR and ALOS-1 PALSAR-1 data were provided by ESA, courtesy of C1F.6504. ALOS-2 PALSAR-2 images were provided by the Japan Aerospace Exploration Agency (JAXA), courtesy of RA4-1058. Sentinel-1 images are available from Copernicus. TanDEM-X data was provided by the German Aerospace Center (DLR), courtesy of Wegmulle_NTI_INSA3397. We thank the anonymous reviewers for their careful reading of our manuscript and their many insightful comments and suggestions.

References

Ambrosi, C., Strozzi, T., Scapozza, C., and Wegmüller, U., 2018. Landslide Hazard Assessment in the Himalayas (Nepal and Bhutan) Based on Earth-Observation Data. Engineering Geologiy, 237: 217-228, doi: 10.1016/j.enggeo.2018.02.020.

Bamler, R. & Hartl, P., 1998. Synthetic Aperture Radar Interferometry. Inverse Problems, 14: R1-R54, doi: 10.1088/0266-5611/14/4/001.

Barboux, C., Delaloye, R. and Lambiel, C., 2014. Inventorying slope movements in an Alpine environment using DinSAR. Earth Surface Processes and Landforms, 39: 2087-2099, doi:10.1002/esp.3603.

Barboux, C., Strozzi, T., Delaloye, R., Wegmüller, U. and Collet, C., 2015. Mapping slope movements in Alpine environments using TerraSAR-X interferometric methods. Journal of Photogrammetry and Remote Sensing, 109: 178-192, doi: 10.1016/j.isprsjprs.2015.09.010.

Barra, A., Solari, L., Béjar-Pizarro, M., Monserrat, O., Silvia Bianchini, S., Herrera, G., Crosetto,

M., Sarro, R., González-Alonso, E., Mateos, R.M., Ligüerzana, S., López, C. and Moretti, S., 2017. A Methodology to Detect and Update Active Deformation Areas Based on Sentinel-1 SAR Images. Remote Sens., 9(10), 1002, doi: 10.3390/rs9101002.

Bernal, I., Tavera, H., and Antahyua, Y., 2002. Zonas sismogénicas en Perú: volúmenes de deformación, gráficos polares y zonificación preliminar. Bol. Soc. Geológica Perú, 93, 31-44.

Blaikie, P., Cannon, T., Davis, I. and Wisner, B., 2014. At Risk: Natural Hazards, People's Vulnerability and Disasters. Evanston, IL: Routledge.

Bianchini, S., Cigna, F. and Casagli, N., 2011. Improving Landslide Inventory with Persistent Scatterers in Calabria, Italy. In: Margottini, C., Canuti, P. and Sassa, K. (eds), Landslide Science and Practice. Springer, Berlin, Heidelberg, doi: 10.1007/978-3-642-31325-7_15.

Bianchini, S., Herrera, G., Mateos, R.M., Notti, D., Garcia, I., Mora, O., and Moretti, S., 2013. Landslide Activity Maps Generation by Means of Persistent Scatterer Interferometry. Remote Sensing, 5, 6198-6222, doi:10.3390/rs5126198.

Bontemps, N., Lacroix, P. and Doin, M., 2018. Inversion of deformation fields timeseries from optical images, and application to the long term kinematics of slow-moving landslides in Peru. Remote Sensing Environment, 210: 144-158, doi: 10.1016/j.rse.2018.02.023.

Casagli, N., Frodella, W., Morelli, S., Tofani, V., Ciampalini, A., Intrieri, E., Raspini, F., Rossi, G., Tanteri, L., and Lu, P. 2017. Spaceborne, UAV and ground-based remote sensing techniques for landslide mapping, monitoring and early warning. Geoenvironmental Disasters, 4: 9, doi: 10.1186/s40677-017-0073-1.

Cigna, F., Bianchini, S. and Casagli, N., 2012. How to assess landslide activity and intensity with Persistent Scatterer Interferometry (PSI): The PSI-based matrix approach. Landslides, 10(3): 267-283, doi: 10.1007/s10346-012-0335-7.

Colesanti, C. & Wasowski, J., 2006. Investigating landslides with space-borne Synthetic Aperture Radar (SAR) interferometry, Engineering Geology, 88(3-4): 173-199. doi:10.1016/j.eng geo.

Crosetto, M., Monserrat, O., Bremmer, C., Hanssen, R., Capes, R. and Marsh, S., 2009. Ground

motion monitoring using SAR interferometry: Quality assessment. European Geologist, 26, 12-15.

Delacourt, C., Allemand, P., Berthier, E., Raucoules, D., Casson, B., Grandjean, P., Pambrun, C. and Varel, E., 2007. Remote-sensing techniques for analysing landslide kinematics: A review. Bull. Soc. Geol. Fr., 178(2), 89-100, doi:10.2113/gssgfbull.178.2.89.

Deere, D.U. & Perez, J.Y., 1985. Remedial measures for large slide movements. Proceedings of the P.R.C.-U.S.-Japan Trilateral Symposium/Workshop on Engineering for Multiple Natural Hazards Mitigation, Beijing, 7-12 January, pp. L-7-1 to L-7-15.

DesInventar, https://www.desinventar.org, last accessed 17.5.2018.

DLR EOC – Earth Observation Center, 2013. TanDEM-X Ground Segment DEM Products Specification Document, Issue 3.0.

Emmer, A., Loarte, E.C., Klimeš, J. and Vilímek, V., 2015. Recent evolution and degradation of the bent Jatunraju glacier (Cordillera Blanca, Peru). Geomorphology, 228: 345-355, doi: 10.1016/j.geomorph.2014.09.018.

Farina, P., Colombo, D., Fumagalli, A., Marks, F. and Moretti, S. 2006. Permanent scatterers for landslide investigations: Outcomes from the ESA-SLAM project. Engineering Geology, 88, 200-217, doi: 10.1016/j.enggeo.2006.09.007.

Ferretti, A., Prati, C., and Rocca, F., 2001. Permanent scatterers in SAR interferometry. IEEE Trans. Geosci. Remote Sens., 39(1): 8-20.

Fídel, L.S., Zavala, B.C., Núñez, S.J., and Valenzuela, G.O., 2006. Estudio de riesgos geológicos del Perú. Franja No. 4. Boletín 29, INGEMMET, Lima, 376 p.

Fiorucci, F., Cardinali, M., Carlà, R., Rossi, M., Mondini, A.C., Santurri, L., Ardizzone, F. and Guzzetti, F. 2011. Seasonal landslide mapping and estimation of landslide mobilization rates using aerial and satellite images. Geomorphology, 129, 59-70, doi: 10.1016/j.geomorph.2011.01.013.

Gonzales, K., Zavala, B., Fruneau, B., Díaz, M., Froger J.L. and Loayza, Y., 2008. Estudios de

zonas de deslizamientos activos en la Cordillera Peruana, aplicando interferometría radar – InSAR. Congreso Peruano de Geología, 14, Congreso Latinoamericano de Geología, 13, Lima, PE, 20 setiembre - 3 octubre 2008, Resúmenes. Lima: Sociedad Geológica del Perú 2008, 6 p.

Guzzetti, F., Mondini, A., Cardinali, M., Fiorucci, F., Santangelo, M. and Chang, K.-T., 2012. Landslide inventory maps: New tools for and old problem. Earth-Science Reviews, 112: 42-66, doi: 10.1016/j.earscirev.2012.02.001.

Harb M. & Dell'Acqua F., 2017. Remote Sensing in Multirisk Assessment: Improving disaster preparedness. IEEE Geoscience and Remote Sensing Magazine, 5(1): 53-65, doi: 10.1109/MGRS.2016.2625100.

Herrera, G., Davalillo, J. C., Mulas, J., Cooksley, G., Monserrat, O. and Pancioli, V., 2009. Mapping and monitoring geomorphological processes in mountainous areas using PSI data: Central Pyreneescase study. Nat. Hazards Earth Syst. Sci., 9, 1587-1598, doi:10.5194/nhess-9-1587-2009.

Huggel, C., Frey, H., Klimeš, J., Strozzi, T., Caduff, R., and Cochachin, A., 2017. Contribution of Earth Observation to landslide early warning. White Paper, Alcantara Study Reference No.: 15/P25, European Space Agency. University of Zurich, Gamma Remote Sensing, National Water Authority Peru, Czech Academy of Sciences: Zurich, pp. 36.

INGEMMET, 1995. Carta Geologica del Perú, 19-h Carhuaz, M 1:100 000, Lima.

INGEMMET, 2000. Estudio de riesgos geológicos del Perú, Franja No. 1. Boletín 23, INGEMMET, Lima, 290 p.

INGEMMET, 2002. Estudio de riesgos geológicos del Perú, Franja No. 2. Boletín 27, INGEMMET, Lima, 368 p.

INGEMMET, 2003. Estudio de riesgos geológicos del Perú, Franja No. 3. Boletín 28, INGEMMET, Lima, 373 p.

INDECI, Instituto Nacional de Defensa Civil, http://www.indeci.gob.pe, last accessed 17 May 2017.

IPCC: Summary for Policymakers. Working Group II Contribution to the IPCC Fifth Assessment Report Climate Change 2014: Impacts, Adaptation and Vulnerability, Cambridge University Press, Cambridge, UK., 2014.

Jay, J., Delgado, F., Torres, J., Pritchard, M., Macedo, O. and Aguilar, V., 2015. Deformation and seismicity near Sabancaya volcano, southern Peru, from 2002 to 2015. Geophysical Research Letters, 42: 2015GL063589, doi: 10.1002/2015GL063589.

Kampherm, T.S., 2009. Landslides triggered by the 1946 Ancash Earthquake (Peru) and geologic controls on the mechanisms of initial rock slope failure. University of Waterloo doctoral dissertation, https://uwspace.uwaterloo.ca/handle/10012/4233, pp 126.

Kasser, G.A., Ames, A. and Zamora, M., 1990. Glacier fluctuations and climate in the Cordillera Blanca, Peru. Ann. Glaciol., 14:136-140. doi: 10.3189/S0260305500008430.

Klimeš, J. & Vilímek, V., 2011. A catastrophic landslide near Rampac Grande in the Cordillera Negra, northern Peru. Landslides, 8:309-320, doi: 10.1007/s10346-010-0249-1.

Klimeš, J., 2012: Geomorphology and natural hazards of the selected glacial valleys, Cordillera Blanca, Peru. Acta Universitatis Carolinae, Geographica, 47(2): 25-31, doi: 10.14712/23361980.2015.14.

Klimeš, J., Vilímek, V. and Benešová, M., 2015. Landslide and glacial lake outburst flood hazard in the Chucchún River basin, Cordillera Blanca, Peru. Acta Universitatis Carolinae, Geographica, 50(2): 173-180, doi: 10.14712/23361980.2015.96.

Klimeš, J., Hartvich, F., Tábořík, P., Blahut, J., Briestensky, M., Stember, J., Emmer, A., Vargas, R. and Balek, J., 2017. Studies on selected landslides and their societal impacts: activity report of the Prague World Centre of Excellence, Czech Republic. Landslides, 14(4): 1547-1553, doi:10.1007/s10346-017-0837-4.

Kunz, M. & Hurni, L., 2008. Hazard Maps in Switzerland – State-of-the-Art and Potential Improvements. In Proceedings of 6th ICA Mountain Cartography Workshop, Lenk, Switzerland, 11–15 February.

Lacroix, P., Zavala, B., Berthier, E. and Audin, L., 2013. Supervised Method of Landslide Inventory Using Panchromatic SPOT5 Images and Application to the Earthquake-Triggered Landslides of Pisco (Peru, 2007, Mw8.0). Remote Sensing, 5(6): 2590-2616, doi:10.3390/rs5062590.

Lacroix, P., Berthier, E. and Maquerhua E. T., 2015. Earthquake-driven acceleration of slow-moving landslides in the Colca valley, Peru, detected from Pliades images. Remote Sensing of Environment, 165: 148-158, doi:10.1016/j.rse.2015.05.010.

Lateltin, O., Haemmig, C., Raetzo, H., and Bonnard, C., 2005. Landslide risk management in Switzerland. Landslides, 2(4): 313-320, doi: 10.1007/s10346-005-0018-8.

Macharé, J., Fenton, C.H., Machette, M.N., Lavenu, A., Costa, C. and Dart, R.L., 2003. Database and map of Quaternary faults and folds in Perú and its offshore region. Open File Report 03-451, USGS, pp. 55.

Martha, T.R., Roy, P., Mazumdar, R.K., Babu Govindharaj, B. and Vinod Kumar, K., 2016. Spatial characteristics of landslides triggered by the 2015 Mw 7.8 (Gorkha) and Mw 7.3 (Dolakha) earthquakes in Nepal. Landslides, 14(2): 697–704. doi:10.1007/s10346-016-0763-x.

Malamud, B., Turcotte, D., Guzzetti, F. and Reichenbach, P., 2004. Landslide inventories and their statistical properties. Earth Surface Processes and Landforms 29: 687-711, doi: 10.1002/esp.1064.

McCalpin, J., 1984. Preliminary age classification of landslides for inventoty mapping. Proceedings 21st annual Enginnering Geology and Soils Engineering Symposium, Moscow, Idaho, 99-111.

MINAM, 2015. Mapa nacional de cobertura vegetal : memoria descriptive. Lima, Perú, p. 105.

Moon, V. & Blackstock, H., 2004. A Methodology for Assessing Landslide Hazard Using Deterministic Stability Models. Natural Hazards, 32: 111, doi: 10.1023/B:NHAZ.0000026793.49052.87.

Nishiguchi, T., Tsuchiya, S. and Imaizumi, F. 2017. Detection and accuracy of landslide movement by InSAR analysis using PALSAR-2 data. Landslides, 14:1483-1490. doi: 10.1007/s10346-017-0821-z.

Ng, A.H.-M., Ge, L., Li, X., Abidin, H.Z., Andreas, H. and Zhang, K., 2012. Mapping land subsidence in Jakarta, Indonesia using persistent scatterer interferometry (PSI) technique with ALOS PALSAR. International Journal of Applied Earth Observation and Geoinformation, 18: 232-242, doi: 10.1016/j.jag.2012.01.018.

Notti, D., Davalillo, J.C., Herrera, G. and Mora, O., 2010. Assessment of the performance of X-band satellite radar data for landslide mapping and monitoring: Upper Tena Valley case study. Nat. Hazards Earth Syst. Sci., 10: 18651875, doi:10.5194/nhess-10-1865-2010.

Petersen, M., Harmsen, S., Jaiswal, K., Rukstales, K., Luco, N., Haller, K., Mueller, C. and Shumway, A., 2017. Seismic Hazard, Risk, and Design for South America. U.S. Geological Survey data release, https://www.sciencebase.gov/catalog/item/58795a8ce4b04df303d97ed8, last accessed 17.5.2018, doi: 10.5066/F7Wm1BK1.

Plafker, G., Ericksen, G.E. and Concha, J.F., 1971. Geological aspects of the May 31, 1970, Peru earthquake. Bull. Seismol. Soc. Am., 61(3):543-578.

Pritchard, M. & Fielding, E., 2008. A study of the 2006 and 2007 earthquake sequence of Pisco, Peru, with InSAR and teleseismic data. Geophysical Research Letters, 35: L09308, doi: 10.1029/2008GL033374.

Raetzo, H., Lateltin, O., Bollinger, D., and Tripet J.P., 2002. Hazard assessment in Switzerland - Codes of practice for mass movements. Bull. Eng. Geol. Env., 61, 263-268, doi: 10.1007/s10064-002-0163-4.

Raetzo, H., & Loup, B., 2016. Protection against Mass Movement Hazards - Guideline for the integrated hazard management of landslides, rockfall and hillslope debris flows. Published by the Federal Office for the Environment FOEN, Bern, Switzerland.

Reynolds Geo-sciences Ltd, 2003. Development of glacial hazard and risk minimisation protocols in rural environments guidelines for the management of glacial hazards and risks. Project No: R7816 (online: HYPERLINK "http://www.bgs.ac.uk/research/international/dfid-kar/add048_col.pdf"http://www.bgs.ac.uk/research/international/dfid-kar/add048_col.pdf).

Righini, G., Pancioli, V. and Casagli, N., 2011. Updating landslide inventory maps using Persistent Scatterer Interferometry (PSI). Int. J. Remote Sens., 33, 1-29, doi: 10.1080/01431161.2011.605087.

Rosen, P., Hensley, S., Joughin, I., Li, F., Madsen, S., Rodriguez, E. and Goldstein, R., 2000. Synthetic Aperture Radar Interferometry. Proceedings of the IEEE, 88(3): 333-382, doi: 10.1109/5.838084.

Sandwell, D., Myer, D., Mellors, R., Shimada, M., Brooks, B. and Foster, J. 2008. Accuracy and Resolution of ALOS Interferometry: Vector Deformation Maps of the Father's Day Intrusion at Kilauea. IEEE Transactions on Geoscience and Remote Sensing, 46(11): 3524-3534, doi: 10.1109/TGRS.2008.2000634.

Sato, H.P. & Harp, E.L., 2009. Interpretation of earthquake-induced landslides triggered by the 12 May 2008, M7.9 Wenchuan earthquake in the Beichuan area, Sichuan Province, China, using satellite imagery and Google Earth. Landslides, 6: 153-159. doi:10.1007/s10346-009-0147-6.

Sepúlveda, S. & Petley, D., 2015. Regional trends and controlling factors of fatal landslides in Latin America and the Caribbean. Nat. Hazards Earth Syst. Sci., 15(8): 1821-1833. doi: 10.5194/nhess-15-1821-2015.

Solari, L., Barra, A., Herrera, G., Bianchini, S., Monserrat, O., Béjar-Pizarro, M., Crosetto, M., Sarro, R. and Moretti S., 2018. Fast detection of ground motions on vulnerable elements using Sentinel-1 InSAR data. Geomatics, Natural Hazards and Risk, 9:1, 152-174, doi: 10.1080/19475705.2017.1413013.

Strozzi, T., Wegmüller, U., Tosi, L., Bitelli, G., and Spreckels, V., 2001, Land subsidence monitoring with differential SAR interferometry, Photogramm. Eng. Remote Sens., 67(11), 1261-1270.

Strozzi, T., Delaloye, R., Kääb, A., Ambrosi, C., Perruchoud, E. and Wegmüller, U., 2010. Combined observations of rock mass movements using satellite SAR interferometry, differential GPS, airborne digital photogrammetry, and airborne photography interpretation.

Journal of Geophysical Research, 115(F01014), doi:10.1029/2009JF001311.

Strozzi, T., Ambrosi, C., and Raetzo, H., 2013. Interpretation of Aerial Photographs and Satellite SAR Interferometry for the Inventory of Landslides. Remote Sensing, 5, 2554-2570, doi:10.3390/rs5052554.

Stumpf, A., Malet, J.P. and Delacourt, C., 2017. Correlation of satellite image time-series for the detection and monitoring of slow-moving landslides. Remote Sensing of Environment, 189: 40-55, doi: 10.1016/j.rse.2016.11.007.

UNISDR: 2009 UNISDR Terminology on Disaster Risk Reduction, United Nations, Geneva, 2009.

USGS, https://earthquake.usgs.gov, last accessed 17.5.2018.

Valderrama Murillo, P.A., Silva Espejo, C., Dueñas Bravo, S. and Araujo Huamán, G., 2016. Peligros geológicos por procesos glaciales, Cordillera Blanca - Río Santa, INGEMMET. Boletín, Serie C: Geodinámica e Ingeniería Geológica 63, 145 p, 11 mapas.

van Westen, C.J., Castellanos, E. and Kuriakose, S.L., 2008. Spatial data for landslide susceptibility, hazard, and vulnerability assessment: An overview. Engineering Geology, 102(3): 112-131, doi: 10.1016/j.enggeo.2008.03.010.

Varnes, D.J., 1978. Slope Movements. Types and Processes. In Landslides: Analysis and Control. Schuster, R.L. and Krizker, R.J., Eds., Spec. Rep. 176, Transp. Res. Board, Nat. Ac. Sc.: Washington, DC, USA.

Varnes, D.J., Radbruch-Hall, D. and Savage, W.Z, 1989. Topographic and Structural Conditions in Areas of Gravitational Spreading of Ridges in the Western United States. USGS Prof. Paper 1496, USGS: Washington, DC, USA, pp. 1-28.

Vilímek V., Zapata. M.L. and Stember, J., 2000. Slope movements in Callejón de Huaylas, Peru. ACTA UNIVERSITATIS CAROLINAE Geographica, 35: 39-51.

Vilímek, V., Zapata, M.L., Klimeš, J., Patzelt, Z. and Santillán, N., 2005. Influence of glacial retreat on natural hazards of the Palcacocha Lake area, Peru. Landslides, 2(2), 107-115. doi: 10.1007/s10346-005-0052-6.

Vilímek, V., Hanzlík, J., Sládek, I., Šandov, M. and Santillán, N., 2012. The Share of Landslides in the Occurrence of Natural Hazards and the Significance of El Niño in the Cordillera Blanca and Cordillera Negra Mountains, Peru. In Sassa, K., Rouhban, B., Briceno, S., McSeveny, M., He, B. (Eds.) Landslides: Global risk prepardness. Springer, 133-148. doi: 10.1007/978-3-642-22087-6_9.

Vilímek, V., Klimeš, J. and Torres, M.Z., 2016. Reassessment of the development and hazard of the Rampac Grande landslide, Cordillera Negra, Peru. Geoenvironmental Disastres, 3:5. doi 10.1186/s40677-016-0039-8.

Villacorta, S., Fídel, L. and Zavala Carrión, B.L., 2012. Mapa de susceptibilidad por movimientos en masa del Perú. Revista de la Asociación Geológica Argentina, 69:393-399.

Wegmüller, U., Werner, C., Strozzi, T., and Wiesmann, A., 2003. Multi-temporal interferometric point target analysis, Proceedings of Multi-Temp 2003 conference, Ispra, Italy.

Wegmüller, U., Bonforte, A., De Beni, E., Guglielmino, F., and Strozzi, T., 2014. Morphological changes at Mt. Etna detected by TanDEM-X. Geophysical Research Abstracts, Vol. 16, EGU.

Weston, R., 2008. Preliminary summary of the Pallcamachay property, Ancash, Peru. Report Strait Gold Corp. Web last visited 29 April 2010.

Wieczorek, G.F., 1984. Preparing a detailed landslide-inventory map for hazard evaluation and reduction. Bulletin of the Association of Engineering Geologists 21(3): 337-342.

Wigmore, O. & Mark, B., 2017. Monitoring tropical debris covered glacier dynamics from high resolution unmanned aerial vehicle photogrammetry, Cordillera Blanca, Peru. The Cryosphere, 11, 2463-2480, doi: 10.5194/tc-11-2463-2017.

Zavala Carrión, B.L., Luque Poma, G., Valderrama Murillo, P.A., Barrantes Huamán, R. and Pari Pinto, W., 2009. Riesgos geológicos en la Región Ancash. INGEMMET, Boletín, Serie C: Geodinámica e IngenieríaGeológica, 38, 280 p.

Zvelebil, J. & Stemberk, J., 2000. Slope monitoring applied to rock fall management in NW Bohemia. In: Bromhead, E., et al. (Ed.), Landslides in Research, Theory and Practice. Proc. 8th Int. Symp. on Landslides, vol. 3. Thomas Telford, London, pp. 1659-1664.

List of Tables and Figures

Table 1. Sensors, frequency band, acquisition dates, time intervals, number of images and of interferograms, and acquisition geometry of the SAR images used for DinSAR and PSI (bold) analyses.

Table 2. Standard statistics of each of the PSI results.

Table 3. Basic characteristics of the geomorphological landslide inventory which covers 28.7 km^2 (27% of the study areas). Debris fl. is debris flow, Temp. in. is temporally inactive, Semi-cir. is semi-circular, NA is not ascertained.

Figure 1. Study area in the Ancash Region, Peru. The red polygons indicate the regions where the geomorphologic landslide inventory was compiled, satellite SAR interferometry was carried out over the entire study area. The stars indicate the positions of the landslides near the villages of Rampac Grande and Marcará. The two black polygons indicate the regions of Figures 7 and 8.

Figure 2. Geology of the study area, L. landslide, dep. deposits and Fm. formation. The four black polygons indicate the regions where the geomorphologic landslide inventory was compiled. The red and orange polygons indicate the Rampac Grande and Marcará landslides, respectively.

Figure 3. Results of PSI analysis with a) ALOS-1 PALSAR-1 for the time period 2007-2011 and the ascending orbit, b) ENVISAT ASAR for the time period 2002-2007 and the descending orbit, c) Sentinel-1 for the time period 2015-2017 and the ascending orbit and d) Sentinel-1 for the for the time period 2014-2017 and the descending orbit. The InSAR-based slope-instability inventory is given by the polygons with their respective deformation rates. The arrows indicate the satellite LOS direction. The black stars indicate the reference points. Areas masked by layover and shadow are in black. The regions where the geomorphologic landslide inventory was compiled are indicated with the white dashed polygons. The locations of the time-series of Figure 5 are shown with letters a to f.

Figure 4. Example of time-series of PSI motion from ALOS-1 PALSAR-1 data for the time period 2007-2011 (a and b), ENVISAT ASAR data for the time period 2002-2007 (c and d), and Sentinel-1 data for the time period 2015-2017 (e, ascending orbit) and 2014-2017 (f, descending orbit). For location, see Figure 3.

Figure 5. Section of the InSAR-based slope-instability inventory on a) ALOS-1 PALSAR-1 PSI for the time period 2007-2011, b) ALOS-1 PALSAR-1 DinSAR of the time period 2007.07.12-2007.08.27, c) ALOS-1 PALSAR-1 DinSAR of the time period 2009.07.17-2009.09.01, d) ALOS-2 PALSAR-2 DinSAR of the time period 2016.02.21-2016.10.02. Landslides discussed in the text are labelled with 1 to 5 in c).

Figure 6. Geomorphologic landslide inventory. Debris fl. is debris flow, Temp. in. is temporally inactive, Semi-cir. is semi-circular, NA is not ascertained.

Figure 7. Sections of (a) the InSAR-based slope-instability inventory and (b) the geomorphological inventory with indication of active and temporally active landslides and debris flows on the ALOS-

1 PALSAR-1 PSI of the ascending orbit for the time period 2007-2011. For location see Figure 1. Regions discussed in the text are labeled with 1 to 4.

Figure 8. Sections in the north-eastern part of (a) the study area of the InSAR-based slope-instability inventory on the ENVISAT ASAR PSI of the descending orbit for the time period 2002-2007 and (b) the geomorphological inventory with indication of active and temporally active landslides and debris flows on the Sentinel-1 PSI of the descending orbit for the time period 2014-2017. For location see Figure 1. The dashed black line indicates the normal fault. Regions discussed in the text are labelled with 1 and 2.

Table 1. Sensors, frequency band, acquisition dates, time intervals, number of images and of interferograms, and acquisition geometry of the SAR images used for DinSAR and PSI (bold) analyses.

Sensor	Band	Acquisition dates	Time intervals	Acquisitions	Interferograms	Geometry
ERS-1/2	C	19960410 - 19990120	35 → 1015 days	7	6	ascending
ERS-1/2	C	19920601 - 20000120	1 → 1459 days	15	6	descending
ENVISAT ASAR	C	20060715 - 20091121	35 → 805 days	13	17	ascending
ENVISAT ASAR	C	20021205 - 20071129	35 → 1820 days	21	8	descending
ALOS-1 PALSAR-1	L	20070109 - 20110307	46 → 1518 days	19	72	ascending
TerraSAR-X	X	20140827 - 20140918	11 → 22 days	3	3	ascending
TerraSAR-X	X	20140830 - 20141002	33 days	2	1	descending
Radarsat-2	C	20140825 - 20141012	24 → 48 days	3	3	ascending
Radarsat-2	C	20140831 - 20141018	24 → 48 days	3	3	descending
ALOS-2 PALSAR-2	L	20141228 - 20170219	56 → 784 days	6	15	ascending
ALOS-2 PALSAR-2	L	20150421 - 20170530	14 → 770 days	6	10	descending
Sentinel-1	C	20150428 - 20170728	12 → 312 days	35	17	ascending
Sentinel-1	C	20141022 - 20170801	12 → 360 days	45	20	descending

Table 2. Standard statistics of each of the PSI results.

Sensor	ALOS-1 PALSAR-1 ascending	ENVISAT ASAR descending	Sentinel-1 ascending	Sentinel-1 descending
Acquisition dates	2007.01.09 - 2011.03.07	2002.12.05 - 2007.11.29	2015.04.28 - 2017.07.28	2014.10.22 - 2017.08.01
Number of scenes	19	21	35	45
Master scene	2010.01.17	2005.03.24	2016.08.20	2016.08.12
Reference point	-77.6452255 E -9.2794371 N	-77.6471634 E -9.2835274 N	-77.6462860 E -9.2808714 N	-77.6452866 E -9.2797432 N
Number of points	60816	4523	69047	42958
Point density	338 PS/km^2	25 PS/km^2	384 PS/km^2	239 PS/km^2
Average rate of motion	-1.51 mm/a	-0.44 mm/a	0.46 mm/a	-0.69 mm/a
Standard deviation	3.39 mm/a	1.53 mm/a	2.96 mm/a	2.35 mm/a
Point motion statistics	%	%	%	%
-100 : -50 mm/a	0.01	0.00	0.00	0.00
-50 : -20 mm/a	0.20	0.00	0.05	0.01
-20 : -10 mm/a	1.42	0.26	0.82	0.76
-10 : -2 mm/a	35.47	7.66	11.10	16.66
-2 : 2 mm/a	54.48	92.09	64.92	76.76
2 : 10 mm/a	8.15	0.00	22.75	5.70
10 : 20 mm/a	0.25	0.00	0.33	0.09
20 : 50 mm/a	0.01	0.00	0.04	0.02
50 : 100 mm/a	0.00	0.00	0.00	0.00

Table 3. Basic characteristics of the geomorphological landslide inventory which covers 28.7 km^2 (27% of the study areas). Debris fl. is debris flow, Temp. in. is temporally inactive, Semi-cir. is semi-circular, NA is not ascertained.

Landslide				Total area (m^2)	No. of landslides	Share of the total landslide area (%)	Average area (m^2)
Type	**Activity**	**Shape**	**Depth**				
Landslide	Active	Planar	Shallow	666,321	38	2	17,085
			Medium	2,404,208	28	8	85,864
	Temp. in.	Planar	Shallow	1,543,502	50	6	30,870
			Medium	4,405,936	32	15	137,685
			Deep	7,719,176	12	27	643,264
		Semi-cir.	Medium	1,982,232	16	7	123,889
			Deep	8,651,416	7	30	1,235,916
Debris fl.	Active	NA	NA	486,570	6	2	81,095
	Temp. in.	NA	NA	865,999	24	3	36,083

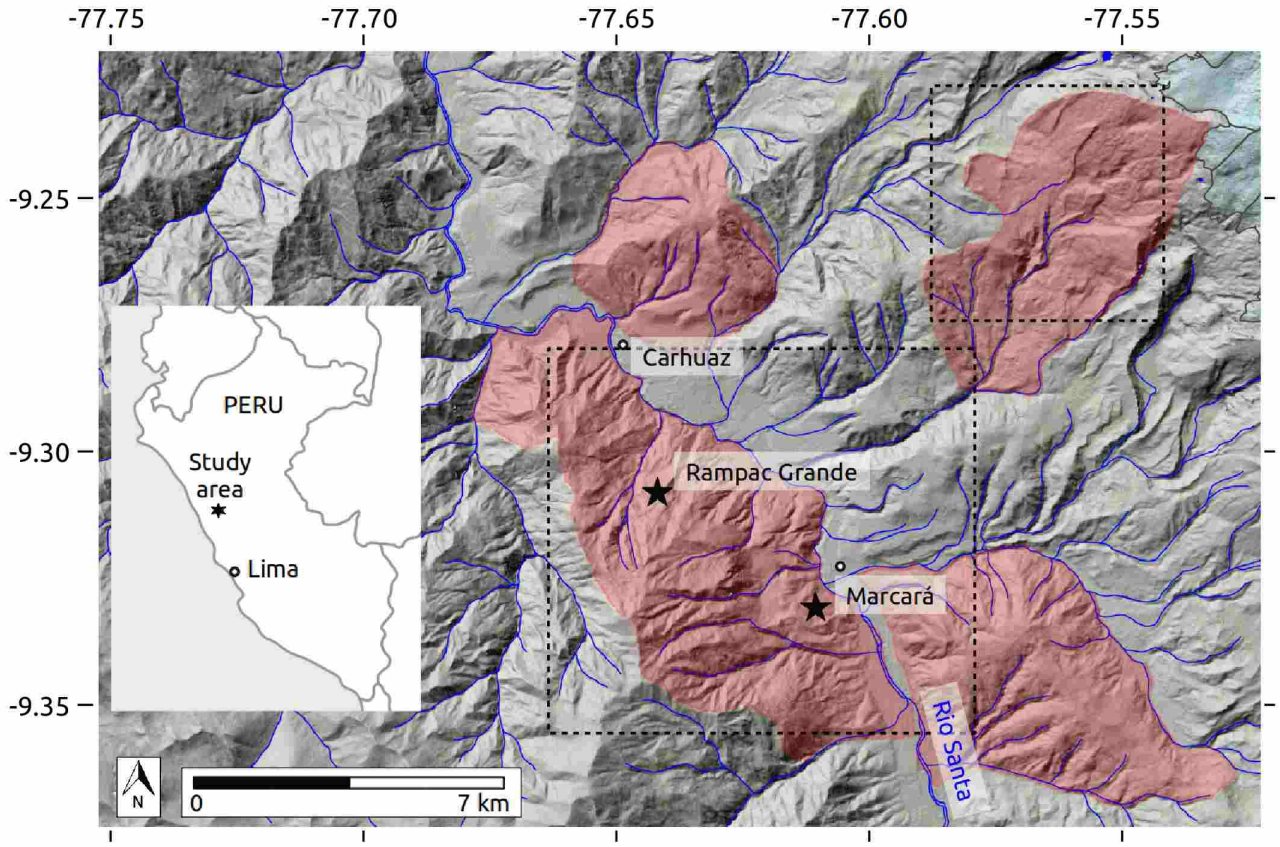

Figure 1. Study area in the Ancash Region, Peru. The red polygons indicate the regions where the geomorphologic landslide inventory was compiled, satellite SAR interferometry was carried out over the entire study area. The stars indicate the positions of the landslides near the villages of Rampac Grande and Marcará. The two black polygons indicate the regions of Figures 7 and 8.

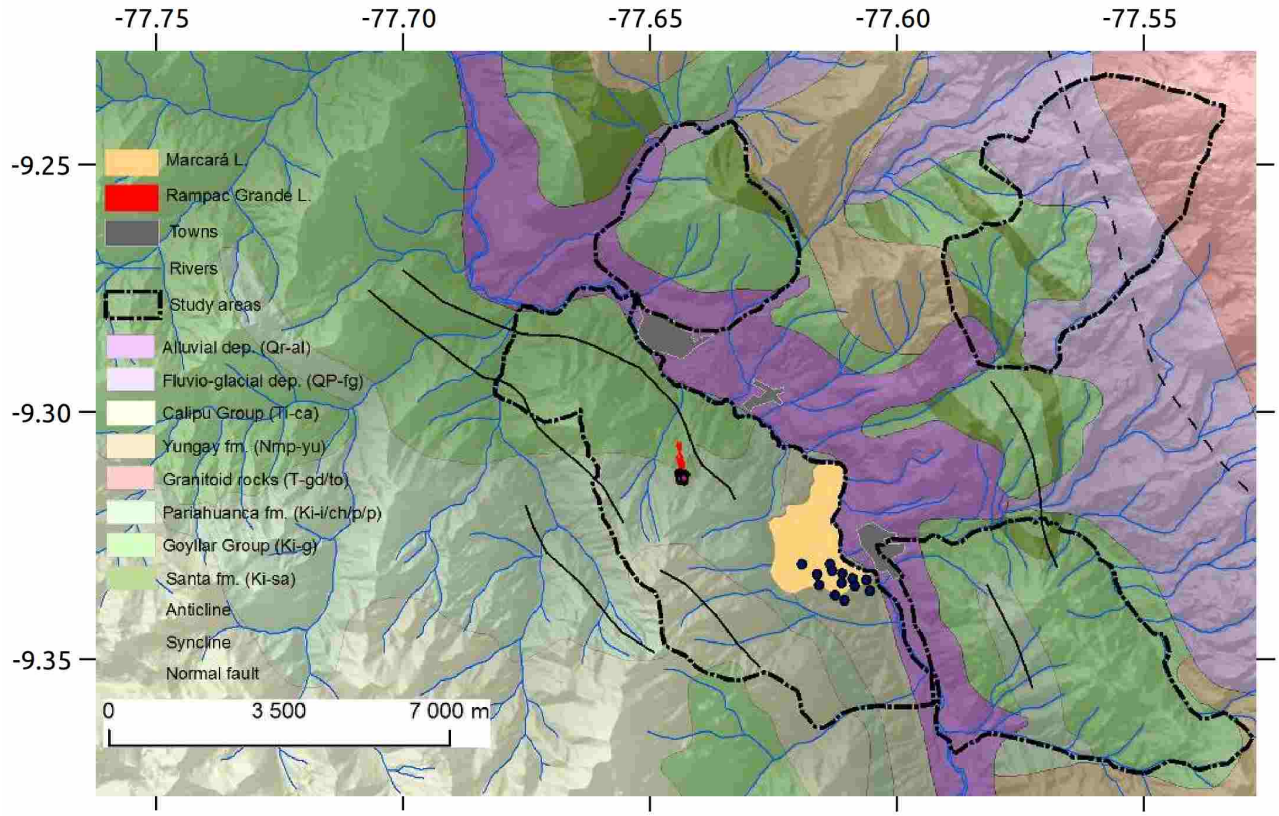

Figure 2. Geology of the study area, L. landslide, dep. deposits and Fm. formation. The four black polygons indicate the regions where the geomorphologic landslide inventory was compiled. The red and orange polygons indicate the Rampac Grande and Marcará landslides, respectively.

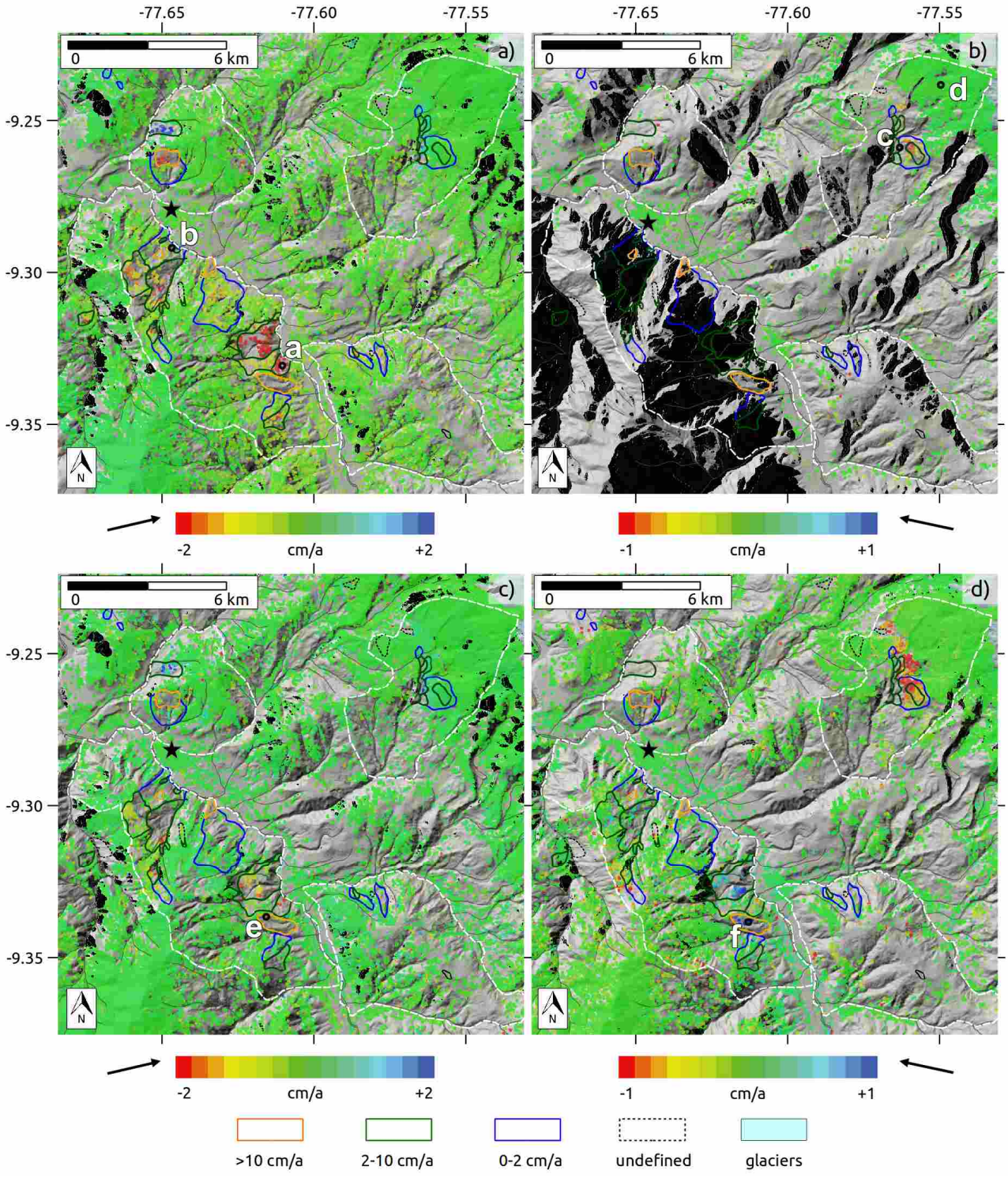

Figure 3. Results of PSI analysis with a) ALOS-1 PALSAR-1 for the time period 2007-2011 and the ascending orbit, b) ENVISAT ASAR for the time period 2002-2007 and the descending orbit, c) Sentinel-1 for the time period 2015-2017 and the ascending orbit and d) Sentinel-1 for the for the time period 2014-2017 and the descending orbit. The InSAR-based slope-instability inventory is

given by the polygons with their respective deformation rates. The arrows indicate the satellite LOS direction. The black stars indicate the reference points. Areas masked by layover and shadow are in black. The regions where the geomorphologic landslide inventory was compiled are indicated with the white dashed polygons. The locations of the time-series of Figure 5 are shown with letters a to f.

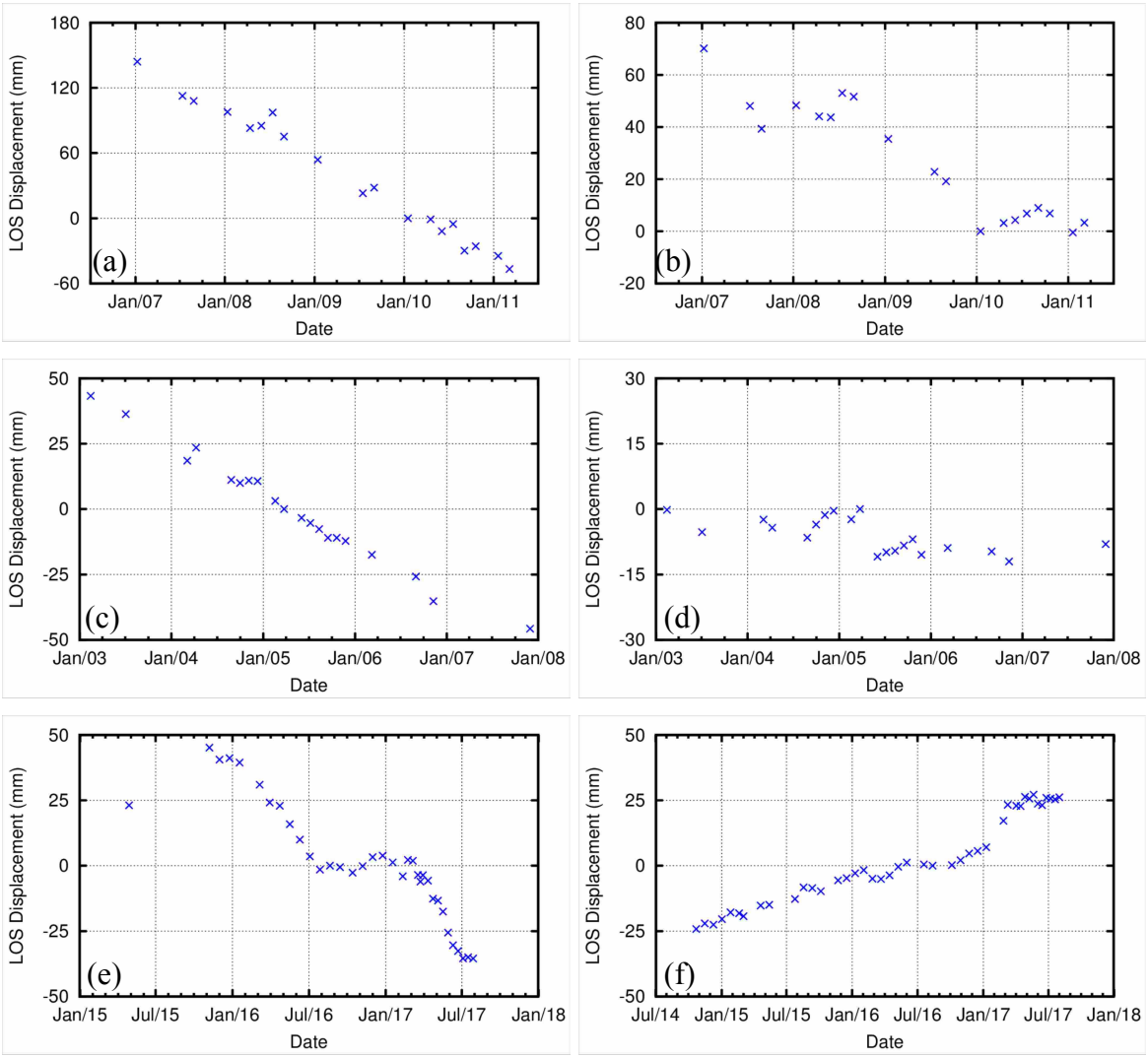

Figure 4. Example of time-series of PSI motion from ALOS-1 PALSAR-1 data for the time period 2007-2011 (a and b), ENVISAT ASAR data for the time period 2002-2007 (c and d), and Sentinel-1 data for the time period 2015-2017 (e, ascending orbit) and 2014-2017 (f, descending orbit). For location, see Figure 3.

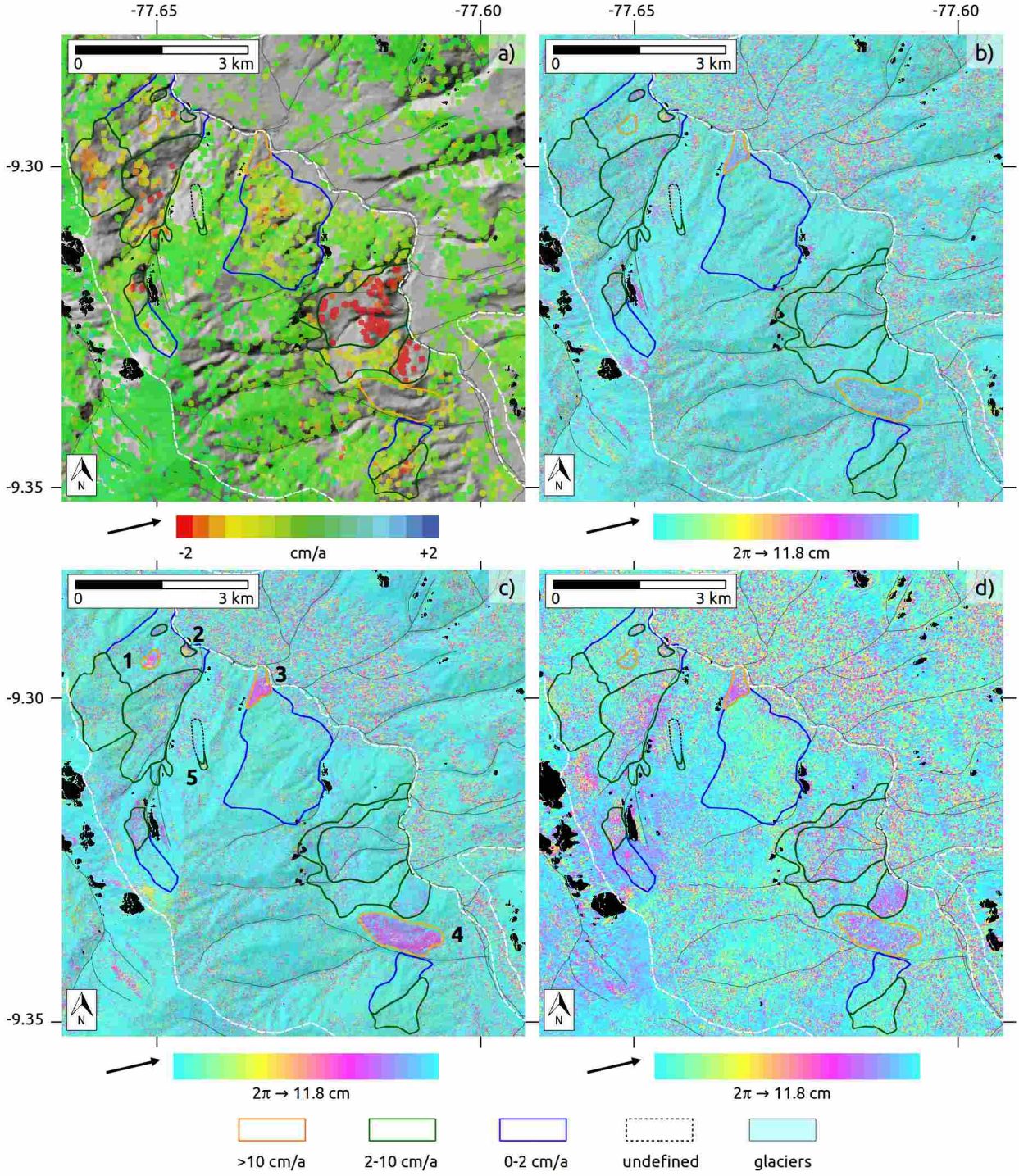

Figure 5. Section of the InSAR-based slope-instability inventory on a) ALOS-1 PALSAR-1 PSI for the time period 2007-2011, b) ALOS-1 PALSAR-1 DinSAR of the time period 2007.07.12-2007.08.27, c) ALOS-1 PALSAR-1 DinSAR of the time period 2009.07.17-2009.09.01, d) ALOS-2 PALSAR-2 DinSAR of the time period 2016.02.21-2016.10.02. Landslides discussed in the text are labelled with 1 to 5 in c).

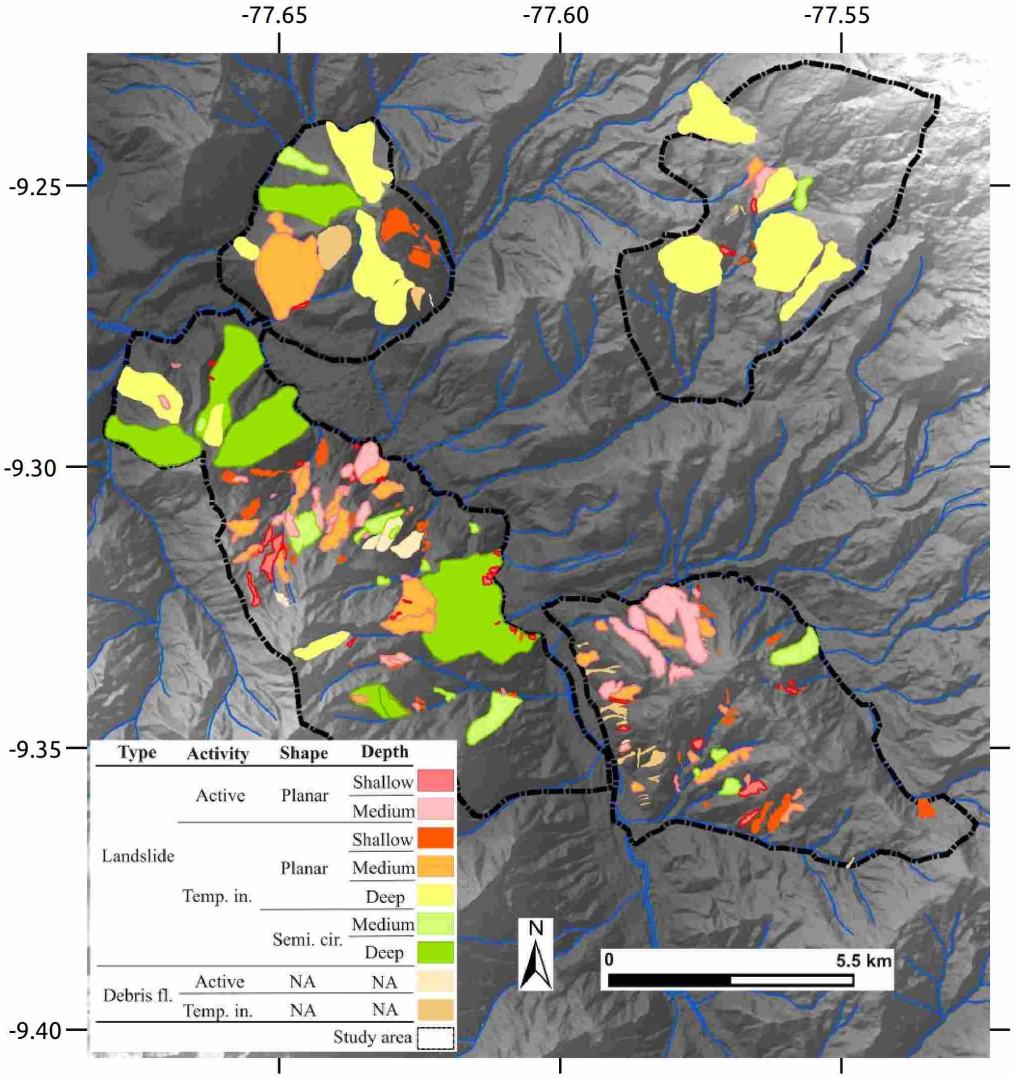

Figure 6. Geomorphologic landslide inventory. Debris fl. is debris flow, Temp. in. is temporally inactive, Semi-cir. is semi-circular, NA is not ascertained.

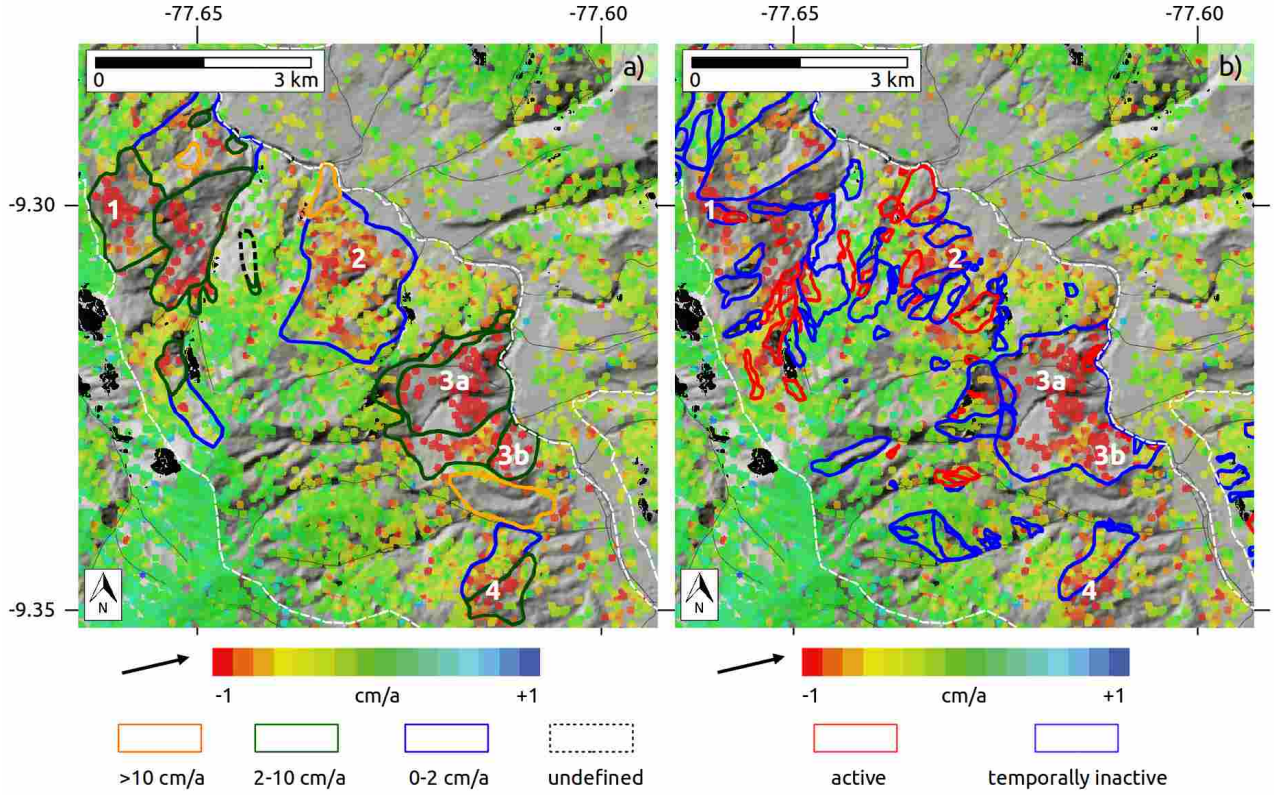

Figure 7. Sections of (a) the InSAR-based slope-instability inventory and (b) the geomorphological inventory with indication of active and temporally active landslides and debris flows on the ALOS-1 PALSAR-1 PSI of the ascending orbit for the time period 2007-2011. For location see Figure 1. Regions discussed in the text are labeled with 1 to 4.

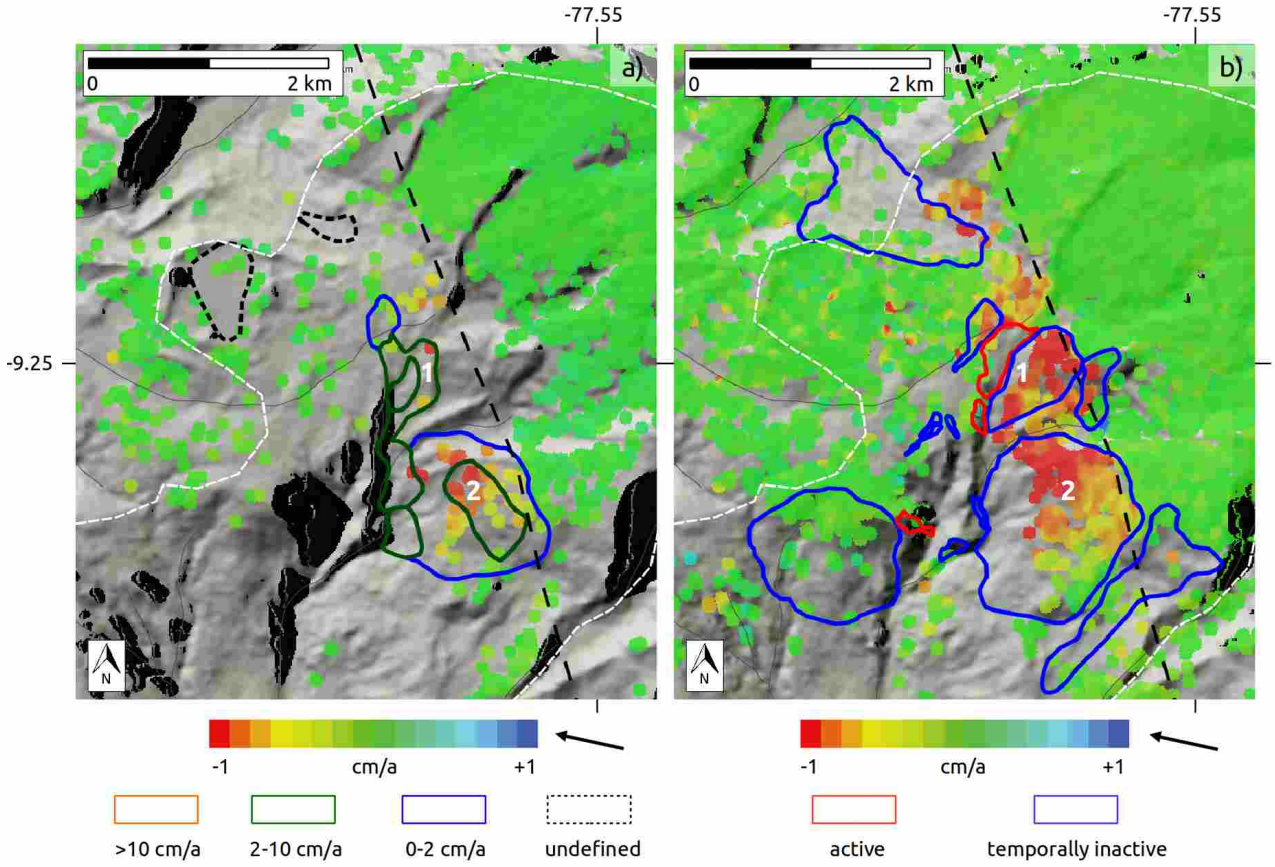

Figure 8. Sections in the north-eastern part of (a) the study area of the InSAR-based slope-instability inventory on the ENVISAT ASAR PSI of the descending orbit for the time period 2002-2007 and (b) the geomorphological inventory with indication of active and temporally active landslides and debris flows on the Sentinel-1 PSI of the descending orbit for the time period 2014-2017. For location see Figure 1. The dashed black line indicates the normal fault. Regions discussed in the text are labelled with 1 and 2.